Improved accuracy of reconstructed diffuse optical tomographic images by means of spatial deconvolution: two-dimensional quantitative characterization

Yong Xu, Harry L. Graber, Yaling Pei, and Randall L. Barbour

Systematic characterization studies are presented, relating to a previously reported spatial deconvolution operation that seeks to compensate for the information-blurring property of first-order perturbation algorithms for diffuse optical tomography (DOT) image reconstruction. In simulation results that are presented, this deconvolution operation has been applied to two-dimensional DOT images reconstructed by solving a first-order perturbation equation. Under study was the effect on algorithm performance of control parameters in the measurement (number and spatial distribution of sources and detectors, presence of noise, and presence of systematic error), target (medium shape; and number, location, size, and contrast of inclusions), and computational (number of finite-element-method mesh nodes, length of filter-generating linear system, among others) parameter spaces associated with computation and the use of the deconvolution operators. Substantial improvements in reconstructed image quality, in terms of recovered inclusion location, size, and contrast, are found in all cases. A finding of practical importance is that the method is robust to appreciable differences between the optical coefficients of the media used for filter generation and those of the target media to which the filters are subsequently applied.

OCIS codes: 170.3880, 170.3010, 100.1830, 100.6950, 100.6890.

1. Introduction

In earlier reports,[1,2] a linear deconvolution strategy was presented that was shown to bring about substantial qualitative improvement in two-dimensional (2D) and three-dimensional (3D) images reconstructed from steady-state (cw) diffuse optical tomographic (DOT) measurement data. The cases that were studied used approximations to measurement geometries commonly employed in DOT mammography[3–6] and in DOT functional brain imaging[7–10] studies, and some took into account the effect of multiplicative noise on the performance of the deconvolution procedure. Among the important questions left unanswered, however, were the limits of spatial resolution and of qualitative (i.e., position, shape, and size of inclusions) and quantitative (i.e., magnitude of recovered absorption and scattering coefficients) accuracy that can be achieved by this method, for different permutations of target, measurement, and computational parameters. Addressing these questions is the subject of the present paper.

As explained in Ref. 2 and subsequently in Section 2, the image-correction process we have devised bears analogies to the use of a physical optics device's point-spread function to sharpen its output, to the calibration of a piece of laboratory equipment with standardized test inputs, or to the localization of radio frequency signals in magnetic resonance imaging (MRI) by means of a frequency-encoding magnetic field gradient. The application of the same concept to DOT image reconstruction entails tagging the optical parameters of each target medium area or volume element in some way. This permits the computation of an information-spread function (ISF) that describes the spatial distribution of the target medium's properties in the reconstructed image. The method used in Refs. 1 and 2 and here is to tag the properties of simulation media voxels by causing them to fluctuate at location-specific frequencies and then to locate and quantify the contribution of each voxel to the

Y. Xu (yong.xu@downstate.edu), H. L. Graber, and R. L. Barbour are with the Department of Pathology, State University of New York Downstate Medical Center, Box 25, 450 Clarkson Avenue, Brooklyn, New York 11203. Y. Pei is with NIRx Medical Technologies LLC, 15 Cherry Lane, Glen Head, New York 11545.

Received 21 July 2004; revised manuscript received 10 November 2004; accepted 11 November 2004.

0003-6935/05/112115-25$15.00/0

reconstructed image by solving a system of linear equations as described in Subsection 2.A.

Specific issues that we examine here include the effect on image quality of varying the number of sources and detectors; the measurement geometry (full tomographic versus limited views); the number of pixels in the inverse-problem mesh; the number and size of regions containing optical parameter values that are different from those of the background (i.e., inclusions); the distance separating multiple inclusions and their distance from the medium boundary; the quantitative inclusion-versus-background optical parameter contrast; and the external geometry of the medium (circular versus rectangular). Also studied was the effect of the discrepancy between the bulk optical parameters of the media used in deriving a deconvolution operator and those of the target medium to which it subsequently is applied. The quality of the images, both before and after application of spatial deconvolution, was quantified by means of several local [i.e., coordinates of inclusion center, inclusion full width at half-maximum (FWHM)] and global (spatial correlation and root-mean-squared difference between medium and image[11]) indices of reconstruction accuracy. Strictly as a matter of convenience with regard to computing the accuracy indices and displaying the results of those computations, the simulation studies conducted here used 2D media.

Although the results obtained in the studies outlined in the previous paragraph are the primary findings for the current report, several other questions related to the method's ultimate limitations, and to its performance relative to other DOT imaging strategies, have been examined as well. These include an attempt to reproduce as nearly as possible an imaging problem considered by Pogue *et al.*,[12] which allows us to compare the performance of the spatial deconvolution approach and a well-characterized iterative nonlinear reconstruction algorithm. As reported below, the iterative algorithm yields a better quantitative (maximum recovered absorption coefficient value) accuracy than the deconvolution approach, but the two have nearly identical qualitative accuracy (inclusion depth and FWHM); thus the net advantage associated with the former method may in some cases be too small to justify its additional computational burden. Furthermore, the comparison suggests that the most efficient approach, in cases in which additional refinement beyond that provided by the deconvolution approach is needed, is to incorporate it into the iterative method to lower the number of iterations required.

2. Methods

A. Spatial Deconvolution Algorithm

The derivation that follows is complementary to that of Ref. 2. Some important properties of the deconvolution operator that are not self-evident in the previously published derivation are made explicit here.

To compute ISFs and deconvolution operators for a given medium, we begin by assigning a fixed numerical ordering to the N_p elements [e.g., nodes in a finite-element-method (FEM) mesh] whose optical parameter values are the inverse-problem unknowns, as indicated in Fig. 1. Then each element, or pixel, is assigned a time-dependent absorption or scattering coefficient, as also indicated in Fig. 1. The particular choice of functional form shown here, and used for the examples subsequently discussed, is a set of sinusoids with incommensurate frequencies, whose amplitudes (ac) were equal to 2% of their mean (dc) values. (For presentation purposes the sinusoids are drawn in Fig. 1 as if they were in phase at time $t = 0$, but in practice a random initial phase shift is assigned to each one.) These optical parameter functions are sampled at a constant interval Δt, until a total number N_t of spatial distributions are recorded. For each of these distributions a forward-problem solution is computed, using a specified fixed set of sources and detectors, such as one of the configurations sketched in Fig. 2 below (see Subsection 2.B). Images of the spatial distributions of medium properties at each of the N_t sample times are reconstructed; the original, or true, and reconstructed spatial distributions of medium optical parameters are accumulated in two $N_p \times N_t$ matrices $\mathbf{Y}$ and $\hat{\mathbf{Y}}$. An important assumption underlying this approach to image enhancement is that the optical parameter information that resides in an individual pixel of the medium is in some manner smeared out within the entire spatial domain of the reconstructed image. (There is no spreading in the temporal dimension because the data from each time slice is processed independently of all the others. Naturally, both spatial and temporal convolution would have to be addressed if an algorithm that simultaneously processes data acquired over many time slices[13,14] were used.) A second assumption is that the contribution of a given medium element to each image element is the same at all times, which is a reasonable expectation if the magnitudes of the optical parameter fluctuations are not large. Then these contributions can be determined by solving a linear system with N_p unknowns: $\mathbf{Y} = \mathbf{F}\hat{\mathbf{Y}}$, where $\mathbf{F}$ is a $N_p \times N_p$ matrix and is called the deconvolution operator or filter, which contains the contri-

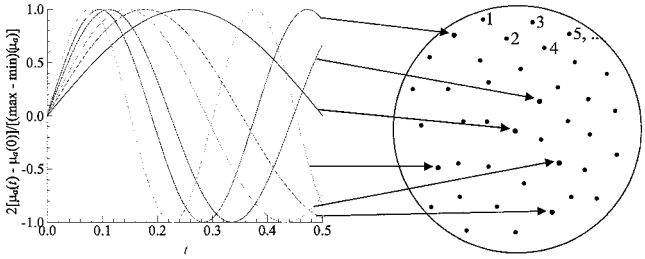

Fig. 1. Schematic illustration of the process of assigning a unique temporal modulation to the absorption or scattering coefficient of each medium pixel. The functional form shown is a set of sinusoids with incommensurate frequencies. For presentation purposes they are drawn as if in phase at time $t = 0$, but in practice a random initial phase shift is assigned to each one.

bution of each medium element to all the image pixels.

In the preceding description, no notice was taken of the ratio N_t/N_p. If $N_t/N_p > 1$, as we have already indicated is the case in practice,[1,2] then $\mathbf{F}$ is the least-squares solution to an overdetermined problem. It follows that the matrices $\mathbf{Y}$ and $\mathbf{F}\hat{\mathbf{Y}}$ are not equal, but that the Frobenius norm of $\mathbf{Y} - \mathbf{F}\hat{\mathbf{Y}}$ is minimized. That is, $\mathbf{F}$ is the transformation that yields the best possible approximation to $\mathbf{Y}$ as a linear combination of rows of $\hat{\mathbf{Y}}$.

Next note that every column in the linear equation $\mathbf{Y} = \mathbf{F}\hat{\mathbf{Y}}$ contains the spatial distributions of optical parameters in the medium and image at a single time slice. Selecting the jth column gives us $\mathbf{Y}(1{:}N_p, j) \approx \mathbf{F}\hat{\mathbf{Y}}(1{:}N_p, j)$, which suggests the manner in which $\mathbf{F}$ can be used to correct reconstruction artifacts resulting from the information-spreading effect of the reconstruction algorithm. Let $\mathbf{z}$ denote the optical parameter values of a target medium that is not in the training set $\mathbf{Y}$. (Note also that, although $\mathbf{Y}$ necessarily consists of simulated media, $\mathbf{z}$ can be a laboratory phantom or other physical structure.) Then we reconstruct the image $\hat{\mathbf{z}}$ from the computed or measured detector readings and then multiply by $\mathbf{F}$ to obtain the corrected image $\hat{\mathbf{z}}' = \mathbf{F}\hat{\mathbf{z}} \approx \mathbf{z}$.

Algebraically, the forward problem for the jth column of the system takes us from the medium with properties $\mathbf{Y}(1{:}N_p, j)$ to the detector data vector $\mathbf{x}_j$; the length of $\mathbf{x}_j$ is the total number of source–detector (S–D) channels. Solving the inverse problem then produces $\hat{\mathbf{Y}}(1{:}N_p, j) = \mathbf{W}^{+}\mathbf{x}_j$, , where $\mathbf{W}$ is the Jacobian or weight matrix and $\mathbf{W}^{+}$ is its pseudo-inverse (including a regularization term, as described in Subsection 2.D). Combining equations for all N_t time slices gives us $\hat{\mathbf{Y}} = \mathbf{W}^{+}\mathbf{X}$, wherein $\mathbf{x}_j$ is the jth column of $\mathbf{X}$. Meanwhile, the system $\mathbf{Y} = \mathbf{F}\hat{\mathbf{Y}}$ has a least-squares solution given by $\mathbf{F} = \mathbf{Y}\hat{\mathbf{Y}}^{+} = \mathbf{Y}\hat{\mathbf{Y}}^{T}(\hat{\mathbf{Y}}\hat{\mathbf{Y}}^{T})^{-1}$. Substituting the preceding expression for $\hat{\mathbf{Y}}$ into this last equation leads to

$$\mathbf{F} = \mathbf{Y}\mathbf{X}^{T}\mathbf{W}^{+T}(\mathbf{W}^{+}\mathbf{X}\mathbf{X}^{T}\mathbf{W}^{+T})^{-1}, \tag{1}$$

which gives the spatial filter operator in terms of the properties of the training set ($\mathbf{Y}$), the corresponding detector data ($\mathbf{X}$), and the image reconstruction algorithm ($\mathbf{W}$).

For the target medium $\mathbf{z}$ with corresponding detector data $\mathbf{v}$, the image $\hat{\mathbf{z}}$ is reconstructed by solving the (usually underdetermined) linear system $\mathbf{v} = \mathbf{W}\mathbf{z}$. Thus $\hat{\mathbf{z}} = \mathbf{W}^{+}\mathbf{v} = \mathbf{W}^{+}\mathbf{W}\mathbf{z}$. Applying the deconvolution operator as described two paragraphs earlier yields

$$\hat{\mathbf{z}}' = [\mathbf{Y}\mathbf{X}^{T}\mathbf{W}^{+T}(\mathbf{W}^{+}\mathbf{X}\mathbf{X}^{T}\mathbf{W}^{+T})^{-1}\mathbf{W}^{+}\mathbf{W}]\mathbf{z}, \tag{2}$$

which gives the dependence of the corrected image on the properties of the training set and the corresponding detector data, the image reconstruction algorithm, and the true properties of the target medium.

Depending on the value of N_p, the overall computation time (N_t forward problems, N_t inverse problems, and solving $\mathbf{Y} = \mathbf{F}\hat{\mathbf{Y}}$) for generation of each deconvolution operator used in the studies is within the range of 1 to 4 h, using a 2.4-GHz processor.

B. Medium and Measurement Geometries for Filter Characterization Studies

As explained in Section 1, although successful application of the image-enhancing procedure has been demonstrated for 3D DOT imaging problems, all computations reported here were carried out on 2D media. As a practical matter, the computation and display of the various indices of reconstruction accuracy (see Subsection 2.E) are more readily carried out in two dimensions. To study the dependence of algorithm performance on all the control variables listed in the Introduction, we have made use of a large set of medium shapes, material properties, finite-element meshes, and S–D configurations. The data presented in Section 3 were obtained from 12 simulation experiments, each designed to examine the dependence of the spatial filtering scheme's performance on a different subset of the control parameters. The parameters that were varied in each of the simulation studies, and the type of inclusions used (i.e., single or multiple, single node or spatially extended), are summarized in Table 1.

The first simulation experiment was a study of the location accuracy, quantitative accuracy, and spatial resolution for a circular medium containing an inclusion that consisted of elevated absorption coefficient μ_a at a single FEM mesh node, as a function of the inclusion's distance from the boundary and of the coarseness of the mesh. In the second, the diameter of the inclusion was varied while its center remained fixed at one of two positions within the medium. In both of these cases the effectiveness of our image-enhancing algorithm on spatial resolution was assessed by computing the FWHM of the inclusion in the reconstructed μ_a image, before and after application of the spatial deconvolution operator, and comparing these with the known diameter of the inclusion in the target medium. In addition, in study 1 the distance between the central point in the recovered inclusion and its known location in the target medium was computed, before and after deconvolution, to quantify the effect of our procedure on location bias.

Studies 3–6 were all concerned with examining the effects of different control parameters on the image-enhancement method's resolving power, for two matched (i.e., having the same diameter and the same μ_a) circular inclusions in a disk-shaped medium: interinclusion separation and coarseness of the FEM mesh (study 3), the number and density of S–D channels (study 4), the inclusions' distance from the boundary (study 5), and the inclusion-versus-background contrast, i.e., the ratio $\mu_a^{\mathrm{incl}}/\mu_a^{\mathrm{bkgr}}$ (study 6).

In the preceding cases, the background optical pa-

Table 1. Control Parameters Considered in the Reported Simulation Experiments

Study Number	Inclusion Properties					Number of FEM Mesh Nodes	Number of S–D Pairs	Noise	Systematic Error	Spatial Versus Recursive Filtering
	Type[a]	Depth	Separation	Size	Contrast					
1	P	✓	—	—	—	✓	—	—	—	—
2	s	✓	—	✓	—	—	—	—	—	—
3	m	—	✓	—	—	✓	—	—	—	—
4	m	—	—	—	—	—	✓	—	—	—
5	m	✓	—	—	—	—	—	—	—	—
6[b]	m	—	—	—	✓	—	—	—	—	—
7	m	—	—	—	—	—	—	—	✓	—
8	s	—	—	—	—	—	—	✓	—	✓
9[b]	m	—	—	—	✓	—	—	—	—	—
10	s, m	—	—	—	—	—	—	—	—	✓
11	s	✓	—	—	—	—	—	—	—	—
12	P	—	—	—	—	—	✓	—	—	—

[a]s = single inclusion, m = multiple inclusions; P = point inclusion (i.e., exactly one FEM mesh node).
[b]The distinction between these two cases lies in the S–D configuration: full tomographic in study 6; limited view in study 9.

rameters of each inclusion-bearing medium were precisely equal to those of the medium used in the corresponding filter-generating computation. However, by employing inclusions whose μ_a values exceed the amplitudes of the tagging functions used in the filter-generation computations, they begin to bear on an important practical consideration. Namely, the robustness of the filtering approach to mismatches between properties of the media, which relates to the question of whether successful application of a computed filter to a physical (laboratory or clinical) target medium can be expected and to the size of the filter library needed to accommodate the probable range of target medium properties. The seventh simulation study reported here more fully addresses the issue of robustness. The single image-correcting filter used here was computed using a medium that had $\langle \mu_a \rangle = 0.002\ \mathrm{mm}^{-1}$ and $\mu_s' = 1.0\ \mathrm{mm}^{-1}$ [where $\langle \mu_a \rangle$ denotes the temporal average value of μ_a], whereas the background μ_a of the heterogeneous test media ranged from 0.0005 to $0.02\ \mathrm{mm}^{-1}$, and their μ_s' ranged from 0.3 to $3.0\ \mathrm{mm}^{-1}$.

The purpose of the eighth experiment was to directly compare the performance of spatial deconvolution and of a well-characterized iterative Newton–Raphson reconstruction algorithm. In this case the same geometries and optical properties of the medium and inclusion as those in Ref. 12 are used for the comparison. Because detector noise was explicitly modeled in Ref. 12, we have included it in our computations as well.

The ninth study was similar to the sixth in that the spatial resolution for two disk-shaped inclusions in a circular medium was examined as a function of $\mu_a^{\mathrm{incl}}/\mu_a^{\mathrm{bkgr}}$; the difference is that here a limited-view S–D distribution was modeled, with all sources and detectors lying along one half of the medium's perimeter. The tenth study is a comparison of the performance of spatial filtering and a recursive iterative reconstruction algorithm for this same S–D configuration.

Additional limited-view studies were conducted in the eleventh and twelfth simulation experiments, where a rectangular FEM mesh was used to determine whether the effectiveness of our image-enhancement approach is strongly influenced by the medium's external geometry. A single-view backreflection measurement was modeled in study 11, a single square-shaped inclusion was employed, and the qualitative and quantitative accuracy of the reconstructed images, before and after application of the spatial filter, was assessed as a function of the distance of the inclusion from the sources and the detectors. A single-view transmission measurement (intended in part to approximate the geometry of the simulation experiment that Markel and Schotland[15] conducted to illustrate the principal conclusions of their paper) was modeled in study 12, the inclusion was a point (one mesh-node) absorber, and the qualitative and quantitative accuracy of the reconstructed images, before and after application of the spatial filter, was assessed as a function of the number and density of sources and detectors.

The various permutations of medium properties used for filter-generation computations are catalogued in Table 2, and the medium geometries, dimensions, and representative S–D distributions are shown schematically in Fig. 2. A point that merits emphasis is that only μ_a was allowed to fluctuate in the simulation studies, whereas the scattering coefficient μ_s' was held constant with a value of $1.0\ \mathrm{mm}^{-1}$. The computations were conducted in this manner only to lower the associated volatile computer memory requirement, and they do not reflect a limitation on the applicability of the method. In fact, μ_s' and μ_a can be simultaneously tagged, and the utility of doing so as a way of quantifying interpa-

Table 2. Properties of Media and S–D Configurations for Which Deconvolution Operators Were Computed[a]

Shape	Dimensions	Measurement Type	Mean μ_a (mm^{-1})	Numbers of Sources (S) and Detectors (D)	Geometric Distribution of S and D Locations	Does S Have a Colocated D?	Numbers of FEM Mesh Nodes and Elements	Study Number
Circle	80-mm diameter	Full tomographic	0.005	16S, 16D (256 channels total)	Uniform, $\Delta\theta_c = 22.5°$	Yes	717/1368	4
				16S, 48D (768)	S: uniform, $\Delta\theta_c = 22.5°$ D: uniform, $\Delta\theta_c = 7.5°$			
							717/1368	1, 3, 4, 5, 6
				32S, 32D (1024)	Uniform, $\Delta\theta_c = 11.25°$		1019/1940	1, 2, 3
							1610/3090	1
			0.002	16 S, 16D, (256)	Uniform, $\Delta\theta_c = 22.5°$		717/1368	7
		Limited view: backreflection	0.005	9S, 24D (216)	S: uniform from $\theta_c = 0°$ to $\theta_c = 180°$, $\Delta\theta_c = 22.5°$ D: three uniformly spaced between pairs of S, $\Delta\theta_c = 5.625°$	No	717/1368	9, 10
	86-mm diameter	Full tomographic	0.01	16S, 16D (256)	Uniform, $\Delta\theta_c = 22.5°$	Yes	1019/1940	8
Rectangle	100-mm wide (X dimension), 60-mm thick (Y dimension)	Backreflection	0.01	33S, 33D (1089)	Uniformly spaced along 100-mm edge, $\Delta X = 2.5$ mm	Yes		11
		Transmission	0.005	9S, 9D (81)	Uniformly spaced along 100-mm edges, $\Delta X = 10$ mm	N/A	1025/1920	12
				17S, 17D (289)	$\Delta X = 5$ mm			
				33S, 33D (1089)	$\Delta X = 2.5$ mm			

[a] θ_c, central angle; $\Delta\theta_c$, central angle interval between adjacent sources or detectors; ΔX, distance between adjacent sources or detectors along the medium surface.

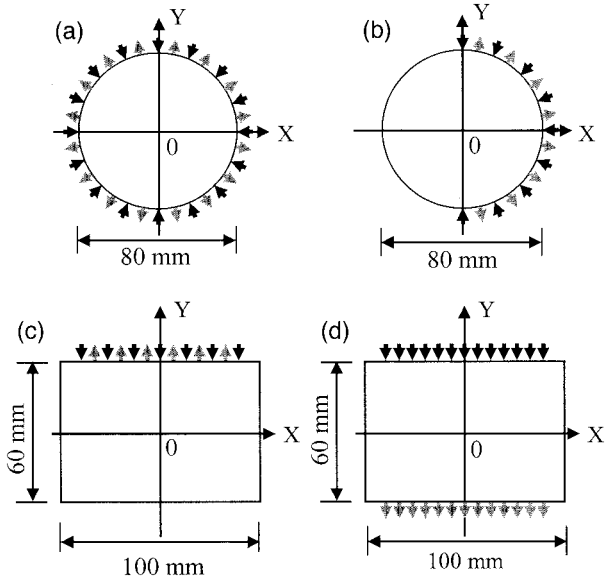

Fig. 2. Medium geometries and S–D configurations used for forward-problem computations, in the filter-generating and filter-testing phases of the reported studies: (a) circular disk, full tomographic measurement (256-channel S–D configuration shown); (b) circular disk, limited-view (backscattering) measurement; (c) rectangular medium, limited-view (backscattering) measurement; (d) rectangular medium, limited-view (transmission) measurement. Indicated S–D locations are only suggestive; see Table 2 for exact numbers and patterning.

rameter cross talk in reconstructed images has been demonstrated.[11]

The simulations that were performed to generate data for the filter application tests used media with the same shapes and dimensions, and with the same S–D configurations, as those in Table 2. The key differences between the filter-generating and filter-testing media are that the latter are static, have spatially heterogeneous absorption, and contain finer FEM meshes than the former. In particular, the circular media used for this part of the studies have meshes with 2771 nodes and 5372 elements, and the rectangular media have meshes with 3969 nodes and 7680 elements. The spatial heterogeneity took the form of discrete inclusions embedded in an otherwise homogeneous background. With the exception of the systematic error study, the background μ_s' was the same as that in the corresponding filter-generating medium, and the background $\mu_a$was equal to the time-averaged value of absorption in the filter-generating medium. The inclusions were regions of elevated μ_a, although they had the same μ_s' as the background. The numbers, dimensions, locations, and other pertinent information about the inclusions are given in Table 3.

C. Solution of the Forward Problem

Tomographic data for the simulated tissue models were acquired by means of the FEM to solve the diffusion equation with Robin boundary conditions for a dc source.[16] For a spatial domain Λ with boundary $\partial\Lambda$, this is represented by the expression

$$\nabla \cdot [D(\mathbf{r})\nabla\phi(\mathbf{r})] - \mu_a(\mathbf{r})\phi(\mathbf{r}) = -\delta(\mathbf{r}-\mathbf{r}_s), \qquad \mathbf{r}\in\Lambda, \tag{3}$$

where $\phi(\mathbf{r})$ is the photon intensity at position $\mathbf{r}$, $\mathbf{r}_s$ is the position of a dc point source, and $D(\mathbf{r})$ and $\mu_a(\mathbf{r})$ are the position-dependent diffusion and absorption coefficients, respectively. Here the definition used for the diffusion coefficient was $D(\mathbf{r}) = 1/\{3[\mu_a(\mathbf{r}) + \mu_s'(\mathbf{r})]\}$, where $\mu_s'(\mathbf{r})$ is the position-dependent scattering coefficient. For all computations considered in this paper, all media had spatially homogeneous and temporally invariant scattering. With the exception of the systematic error study (study 12; see Table 1), the value of the scattering coefficient was $\mu_s' = 1.0\ \mathrm{mm}^{-1}$.

Imaging operators (see Subsection 2.D) were computed, in the manner described in Ref. 16, for each S–D channel. In brief, each row of the matrix $\mathbf{W}_r$ [Eqs. (4) and (5), below] is a function of two forward-problem solutions: a product of forward and adjoint intensities for perturbations of μ_a and a dot product of forward and adjoint intensity gradients for perturbations of D. For each combination of medium geometry and S–D configuration, a single set of imaging operators was used for all inverse-problem computations. These were computed for a homogeneous reference medium with the same shape, size, and measurement geometry as the (heterogeneous) target and with optical parameters equal to the background values of those in the target.

D. Solution of the Inverse Problem

The reconstruction algorithm that was used to generate the results presented in Section 3 solves a regularized modified perturbation equation, by computing

$$\delta\mathbf{x} = \mathbf{W}_r^T(\mathbf{W}_r\mathbf{W}_r^T + \lambda\mathbf{I})^{-1}\delta\mathbf{I}_r, \tag{4}$$

or

$$\delta\mathbf{x} = (\mathbf{W}_r^T\mathbf{W}_r + \lambda\mathbf{I})^{-1}\mathbf{W}_r^T\delta\mathbf{I}_r, \tag{5}$$

depending on whether the overall number of S–D channels N_c is less than [Eq. (4)] or greater than [Eq. (5)] N_p. In these equations $\delta\mathbf{x}$ is the vector of differences between the optical properties (e.g., absorption and scattering or diffusion coefficients) of a measured target and a defined reference medium; $\mathbf{W}_r$, the imaging operator or weight matrix, is the matrix describing the influence that each voxel has on the surface detectors for the selected reference medium; λ is the zero-order Tikhonov regularization parameter (the numerical value used for all inverse-problem computations was $\sim$0.05);[17] and $\delta\mathbf{I}$ is proportional to the difference between detector readings obtained from the target in two distinct states (e.g., difference between data collected at two different instants, or

Table 3. Properties of Inclusions Used in Deconvolution Procedure Characterization Simulations

Medium and Measurement Type	Inclusion Properties: Number	Shape	Dimensions[a] (mm)	Coordinates of Center (mm)	μ_a (mm^{-1}); $\mu_a^{incl}/\mu_a^{bkgr}$	Study Number
80-mm-diameter circle		Point (one FEM mesh node)	~1.6[b]	$X = 0-35$ ($\Delta X = 1$), $Y = 0$	0.02; 4	1
Full tomographic	1	Circle	2, 6, 8, 10, 15, 20 2, 6, 8, 10, 15, 18	$X = 10, Y = 0$ $X = 30, Y = 0$	0.01; 2	2
	2	Circle	6	$X_1 = -5, X_2 = 5, Y = 0$ $X_1 = -7, X_2 = 7, Y = 0$ $X_1 = -10, X_2 = 10, Y = 0$ $X_1 = -7, X_2 = 7, Y = 15$ $X_1 = -7, X_2 = 7, Y = 25$	0.01; 2	3 3, 5 3, 4 5
	4		10	$X_1 = -10, X_2 = 10, Y = 15$	0.0075; 1.5 0.01; 2 0.015; 3	6
			6	$X_1 = 15, X_{2,3} = 0, X_4 = 15,$ $Y_{1,4} = 0, Y_2 = -15, Y_3 = 15$	see Fig. 11; 2	7
Limited view	1	Circle	6	$X = 15, Y = 0$	0.01; 2	10
	2			$X = 0, Y_1 = -15, Y_2 = 15$	0.006; 1.2 0.01; 2 0.02; 4 0.04; 8	9 9, 10 9
86-mm-diameter circle Full tomographic	1	Circle	20	$X = 15, Y = 0$	0.02; 2	8
Rectangle, backreflection	1	Square	10×10	$X = 0, Y = 20$ $X = 0, Y = 10$ $X = 0, Y = 0$ $X = 0, Y = -10$	0.02; 2	11
Rectangle, transmission	1	Point (one FEM mesh node)	~1.6[b]	$X = 0, Y = 0$	0.02; 2	12

[a]Tabulated dimension is the diameter for circular inclusions, length × width for rectangular and square inclusions.
[b]This approximate linear dimension is the square root of the mean area of the forward-problem finite elements.

the difference between instantaneous and time-averaged data).

The distinction between Eqs. (4) and (5) and a standard linear perturbation equation lies in the structure of the term $\delta\mathbf{I}_r$ on the right-hand side. Here we used the previously described normalized difference method (NDM),[18] in which $\delta\mathbf{I}_r$ is defined by

$$(\delta\mathbf{I}_r)_i = \frac{(\mathbf{I} - \mathbf{I}_0)_i}{(\mathbf{I}_0)_i} (\mathbf{I}_r)_i. \tag{6}$$

In Eq. (6), $\mathbf{I}_r$ is the computed detector readings corresponding to a selected reference medium. For the filter-generating computations, $\mathbf{I}$ and $\mathbf{I}_0$ represent the intensity at a specific time point and the time-averaged intensity, respectively, whereas the medium used for the $\mathbf{I}_r$ computation has the same μ_s' as, and μ_a equal to the time-averaged value for, the filter-generating medium. For the filter-testing computations, $\mathbf{I}$ and $\mathbf{I}_0$ are the intensities (i.e., detector readings) computed for the heterogeneous target medium and a homogeneous medium with optical coefficients identical to those of the target medium's background region,[19] respectively, and $\mathbf{I}_r$ is identical to $\mathbf{I}_0$.[20]

A Levenberg–Marquardt (LM) algorithm was used to compute numerical solutions to Eqs. (4) and (5).[21] In these computations, the $\delta\mathbf{x}$ that was solved for included position-dependent perturbations in both μ_a and D. No use was made of any *a priori* information regarding the spatial distributions of either coefficient. Thus the number of unknowns in each inverse-problem computation was twice the number of mesh nodes. Accordingly, the dimensions of the quantities in Eqs. (4) and (5) are $N_c \times (2N_p)$ for $\mathbf{W}_r$, $N_c \times 1$ for $\delta\mathbf{I}_r$, and $(2N_p) \times 1$ for $\delta\mathbf{x}$.

Most of the characterization studies made use of noise-free data. Since the robustness of the deconvolution method to detector noise was already examined in Ref. 2, neglecting noise effects in the present paper is not an oversight. However, in the case of study 8 (see Subsection 2.B and Table 1) the decision to include noise was taken to reproduce as closely as possible the conditions of a computation reported in Ref. 12. Accordingly, the detector readings were corr-

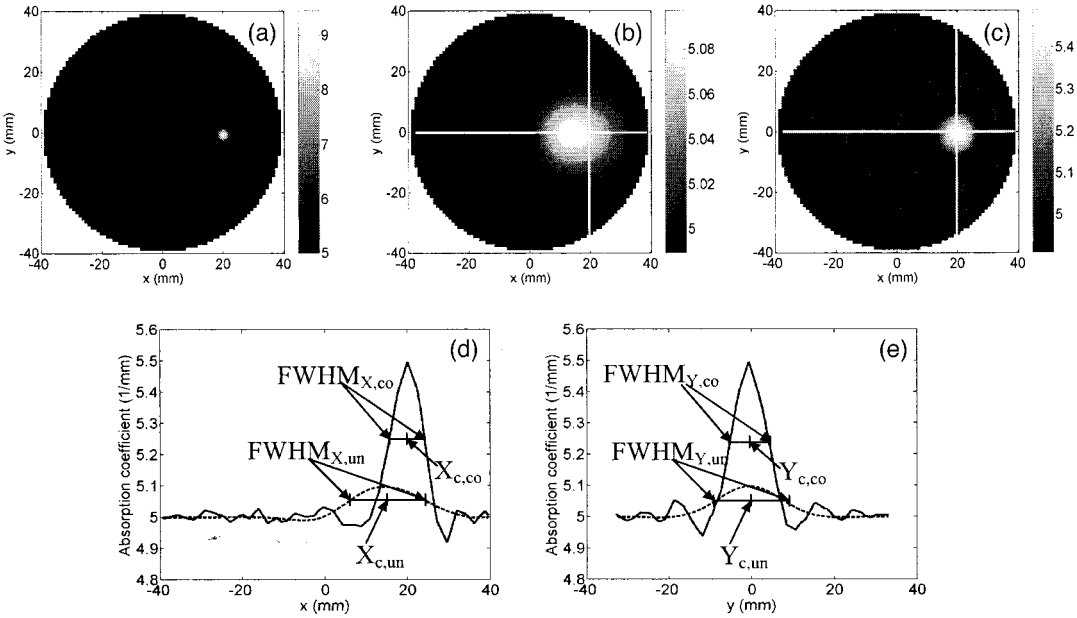

Fig. 3. Study 1: definitions of spatial resolution and of inclusion center coordinates for reconstructed images. (a) Point-like inclusion located at (20, 0) mm; (b) image before deconvolution; (c) image after deconvolution; (d) 1D recovered μ_a distribution along $y = 0$ before (dashed curve) and after (solid) deconvolution; (e) μ_a distribution along $x = 20$ mm. Gray-scale [(a)–(c)] and ordinate axis [(d), (e)] values are $1000 \times \mu_a$.

upted with multiplicative Gaussian noise at a uniform level of 1%; that is, the noise–vector element corresponding to the ith S–D channel was sampled from the Gaussian distribution $N(0, 0.01(\mathbf{I}_0)_i)$. Then $\mathbf{I}' = \mathbf{I} + \mathbf{n}$, where $\mathbf{n}$ is the noise vector, was substituted for $\mathbf{I}$ in Eq. (6).

E. Quantification of Reconstructed Image Quality and Accuracy

For the first simulation study, in which the inclusion consisted of a single FEM mesh node, the qualitative accuracy of the recovered images, before and after application of the spatial deconvolution step, was assessed by computing two "local" indices of agreement between image and target media: the inclusion's FWHM and the absolute error in the (X, Y) coordinates of its center. The manner in which these quantities are defined for this paper are illustrated in Fig. 3. Shown in Figs. 3(a)–3(c) are the spatial distributions of μ_a in a selected target medium, in the image reconstructed by solving Eq. (4) or (5), and in the corrected image that is obtained by applying Eq. (2), respectively. The curves plotted in Figs. 3(d) and 3(e) are the recovered μ_a along the one-dimensional (1D) sections shown as white solid lines in Figs. 3(b) and 3(c); the white lines intersect at the known coordinates of the mesh node with elevated μ_a. As indicated in Figs. 3(d) and 3(e), the maximal and baseline values of recovered μ_a ($\mu_a^{\max}$ and μ_a^{bkg}, respectively) are identified in each of the 1D sections, after which the two positions $X_{50,1}$ and $X_{50,2}$ for which $\mu_a = (\mu_a^{\max} - \mu_a^{\mathrm{bkg}})_x/2$, and the two positions $Y_{50,1}$ and $Y_{50,2}$ for which $\mu_a = (\mu_a^{\max} - \mu_a^{\mathrm{bkg}})_Y/2$ are found. The FWHM values shown in Section 3 are defined as $\mathrm{FWHM}_X = |X_{50,2} - X_{50,1}|$, $\mathrm{FWHM}_Y = |Y_{50,2} - Y_{50,1}|$, and the inclusion center coordinates are defined as $(X_c, Y_c) = ([X_{50,2} + X_{50,1}]/2, [Y_{50,2} + Y_{50,1}]/2)$. The results of these computations do not differ appreciably from those obtained by finding the center of mass and the average radius of the image's μ_a spatial distribution.[11]

The absolute errors $E_X = |X_{c,\mathrm{img}} - X_{c,\mathrm{tgt}}|$ and $E_Y = |Y_{c,\mathrm{img}} - Y_{c,\mathrm{tgt}}|$, where "img" and "tgt" denote the reconstructed image and target medium, respectively, were computed for both the uncorrected and corrected images. The spatial filtering operation is deemed to have a beneficial effect on qualitative accuracy if it leads to reductions in E_X, E_Y, FWHM_X, and FWHM_Y.

The quantitative image accuracy in the case of study 1 was assessed via direct comparisons of $\mu_a^{\max}$ and μ_a^{bkg} of the target medium and the uncorrected and corrected reconstructed images. The spatial filtering operation is deemed to have a beneficial quantitative effect if it leads to reductions in both $|\mu_{a,\mathrm{img}}^{\max} - \mu_{a,\mathrm{tgt}}^{\max}|$ and $|\mu_{a,\mathrm{img}}^{\mathrm{bkg}} - \mu_{a,\mathrm{tgt}}^{\mathrm{bkg}}|$.

For the simulation studies that made use of one or more spatially extended inclusions, the effect of spatial filtering on qualitative accuracy was assessed by computing the increase in spatial correlation r_s between the target and image, and the effect of spatial filtering on quantitative accuracy was assessed by computing the decrease in the root-mean-squared error (RMSE) ε between the target and the image.[11] The formulas defining these "global" indices of agreement between image and target media are

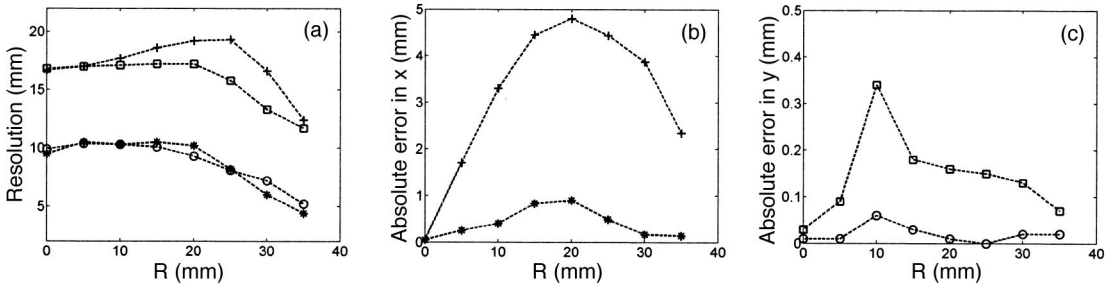

Fig. 4. Study 1: position dependence of spatial resolution and absolute location error of recovered images. (a) Image resolution, in which curves with + and □ markers are the FWHM_X and FWHM_Y, respectively, before deconvolution, and curves with * and ○ symbols are the FWHM_X and FWHM_Y, respectively, after deconvolution; (b) inclusion's absolute location error E_X before (+) and after (*) deconvolution; (c) absolute location error E_Y before (□) and after (○) deconvolution. The mesh and S–D geometry are the same as in Fig. 3.

$$r_s = \frac{\sum_{i=1}^{N_p} (\mu_{a,\mathrm{img}}{}^i - \overline{\mu}_{a,\mathrm{img}})(\mu_{a,\mathrm{tgt}}{}^i - \overline{\mu}_{a,\mathrm{tgt}})}{\left[\sum_{i=1}^{N_p} (\mu_{a,\mathrm{img}}{}^i - \overline{\mu}_{a,\mathrm{img}})^2 \cdot \sum_{i=1}^{N_p} (\mu_{a,\mathrm{tgt}}{}^i - \overline{\mu}_{a,\mathrm{tgt}})^2\right]^{1/2}}, \quad (7)$$

(where $\overline{\mu}_a$ denotes the spatial average value of μ_a) and

$$\varepsilon = \left[\frac{1}{N_p} \sum_{i=1}^{N_p} (\mu_{a,\mathrm{img}}{}^i - \mu_{a,\mathrm{tgt}}{}^i)^2\right]^{1/2}, \quad (8)$$

respectively.

Careful inspection of Figs. 3(b)–3(e) reveals two additional features that must be taken into account for proper interpretation of r_s and ε data. One is the presence of the analogue of ringing artifacts[22] about the inclusion, the amplitudes of which are larger in the corrected than in the uncorrected images. Although algorithms for the suppression of such artifacts are available,[23] none was used in generating results presented in this paper in order to avoid the introduction of confounding variables. The second is that the peak value of the recovered absorption contrast, although five times larger in the corrected versus the uncorrected images, is not close to the 4:1 ratio present in the target medium in either result. Consequently, it is not realistic to expect numerical values of r_s and ε to be close to the theoretical ideals of 1 and 0, respectively. As a practical matter, the percentage increase in r_s and decrease in ε after the application of spatial deconvolution are more meaningful measures of that operation's effectiveness.

3. Results

As outlined above in Subsection 2.B, the first simulation study was concerned with resolution limits and accuracy of images of (circular, full tomographic measurement) target media in which the inclusion consisted of a single node in the forward-problem FEM mesh (with μ_a and absorption contrast fixed; see Table 3). Intuitively it would seem that the finest spatial resolution achievable is determined by the distance between nodes in the inverse-problem FEM mesh, whereas the smallest possible location error should be the distance between the perturbed node in the forward-problem mesh and the nearest inverse-problem mesh node, when the two meshes are overlaid. In practice, of course, the location error and resolution actually achieved can be considerably worse than these limiting values. An example of this is seen in Fig. 3(b), in which the absolute location error E_X and the resolution indices FWHM_X and FWHM_Y are all noticeably greater than the internode separation. To explore this further, we computed the four quantities E_X, E_Y, FWHM_X, and FWHM_Y as a function of the location of the perturbed node on the X axis [see Fig. 2(a)], which ranged from 0 to 35 mm at intervals of 5 mm. At each position along the X axis, the node used as the inclusion was the one whose Y coordinate was closest to zero. In Fig. 4 we show plots of FWHM_X and FWHM_Y, E_X, and E_Y, versus the distance from the medium center for both uncorrected and corrected reconstructed images. These data were obtained when a fixed 1024-channel S–D configuration and a fixed 1019-node inverse-problem mesh were used.

The most striking feature of Fig. 4 is that all four local accuracy indices are smaller (i.e., better, with the ideal value being zero) in the corrected image, for all positions of the inclusion. This was not unexpected, at one level, given the previous demonstrations of image enhancement. However, the results provide a previously unavailable quantification of the degree of improvement achieved. For example, when $X = 20$ mm we find that E_X declines from 4.8 to 0.8 mm (83% decrease), E_Y from 0.16 to 0.01 mm (94%), FWHM_X from 19.2 to 10.2 mm (47%), and FWHM_Y from 17.2 to 9.2 mm (47%). Also of interest is the trends seen in the curves. Resolution [Fig. 4(a)] either remains nearly constant or slowly worsens with increasing distance from the center when the inclusion lies closer to the center than to the boundary, but it rapidly improves with increasing distance from the center once the inclusion has passed the halfway point—a not unexpected boundary layer effect (see Section 4). The location error E_X [Fig. 4(b)] has a maximum value at $X = 20$ mm, decreasing as the inclusion approaches either the center or the boundary. This trend is consistent with the behavior of optical tomographic reconstruction algorithms as observed by many groups[24,25]: Recovered superficial features are displaced toward the boundary, whereas

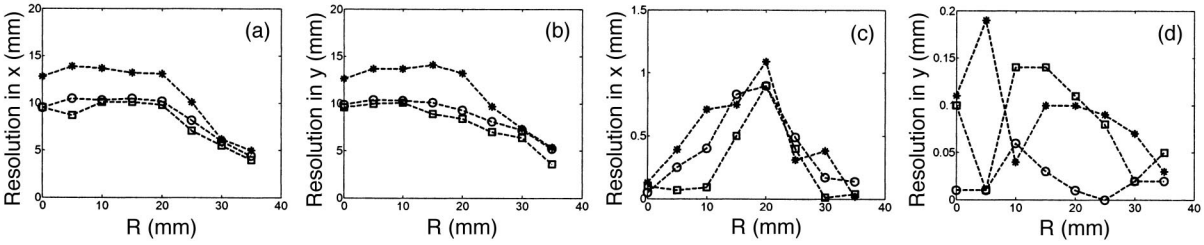

Fig. 5. Study 1: resolution and absolute location error of recovered inclusion for three different meshes. (a) FWHM_X; (b) FWHM_Y; (c) E_X; (d) E_Y. All results shown are for deconvolved images; *, ○, and □ labels denote results for 717-, 1019-, and 1610-node meshes, respectively. The same medium and S–D geometry used in Fig. 3 were also used here.

deep ones are displaced toward the region of lowest weight [Eqs. (4) and (5)], which typically is at the center for a full tomographic measurement. Finally, the curves plotted in Fig. 4(c) indicate a maximum in the location error E_Y when $X = 10$ mm. However, additional data presented next demonstrate that this maximum is an idiosyncratic feature of the particular FEM mesh that was used for the inverse-problem computations.

The remainder of study 1 involved repeating the entire set of computations an additional two times while using different inverse-problem meshes—one coarser ($N_p = 717$) and the other finer ($N_p = 1610$)—than the 1019-node mesh that produced the data shown in Fig. 4. Plots of the four local accuracy indices of the corrected images and for all three meshes, as a function of location of the perturbed node on the X axis, are shown in Fig. 5. In every case, all four plotted indices are smaller than the corresponding values for the uncorrected images (which are not plotted here). Inspection of the resolution curves in Fig. 5(a) reveals that both FWHM_X and FWHM_Y improve as the mesh becomes finer and that both exhibit a boundary layer effect at all values of N_p. The former phenomenon was expected, in light of the reduction in the average internode distance $\overline{\Delta s}$ with increasing N_p, but the magnitude of the improvement in resolution is not proportional to the percentage decrease in $\overline{\Delta s}$. Instead, a larger improvement in resolution is achieved by increasing N_p from 717 to 1019 ($\overline{\Delta s}$ decreases by 0.17 mm) than by increasing it from 1019 to 1610 ($\overline{\Delta s}$ decreases by 0.19 mm); this may be associated with the transition from overdetermined to underdetermined inverse problems that occurs when N_p exceeds the total number of S–D channels (1024), or it may be indicative of a fundamental limit to the spatial resolution of DOT reconstructed images. The existence of such a limit is not unexpected, in light of the analytical findings reported by Markel and Schotland.[15]

Inspection of the E_X-versus-X curves in Fig. 5(c) reveals that they all have similar qualitative forms, with the location error maximal for an inclusion at $X = 20$ mm for all three meshes but decreasing with increasing N_p for almost all inclusion positions. On the other hand, comparison of the E_Y-versus-X curves for the three meshes indicates that there is no consistent pattern to the dependence of E_Y on the position of the inclusion on the X axis. The range of values plotted along the ordinate in Fig. 5(d) is an order of magnitude smaller than that on the corresponding axis of Fig. 5(c). Presumably, repeating all computations using the same three values of N_p, but different geometrical arrangements of the nodes, would yield a completely different set of E_Y curves. It is our expectation that detailed features such as the crossings of the $\mathrm{FWHM}_{X,\mathrm{cor}}$ and $\mathrm{FWHM}_{Y,\mathrm{cor}}$ curves in Fig. 4(a) would likewise prove to be idiosyncratic.

Inclusions of finite diameter d (2–20 mm) were modeled in the second simulation experiment, the point of which was to characterize the accuracy with which the inclusion size can be recovered. The principal result is shown in Fig. 6, in which we plot $\mathrm{FWHM}_{X,\mathrm{cor}}$ versus d [Fig. 6(a)] and $\mathrm{FWHM}_{Y,\mathrm{cor}}$ versus

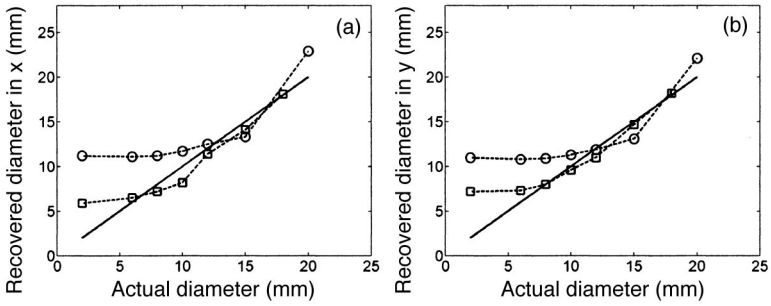

Fig. 6. Study 2: FWHMs for finite-diameter inclusions. (a) FWHM_X versus true diameter and (b) FWHM_Y versus true diameter. Results shown are for corrected images; curves with □ and ○ symbols are the results for inclusion centered at (30, 0) mm and at (10, 0) mm, respectively; solid lines are ideal results. The same mesh and S–D geometry used in Fig. 3 were also used here.

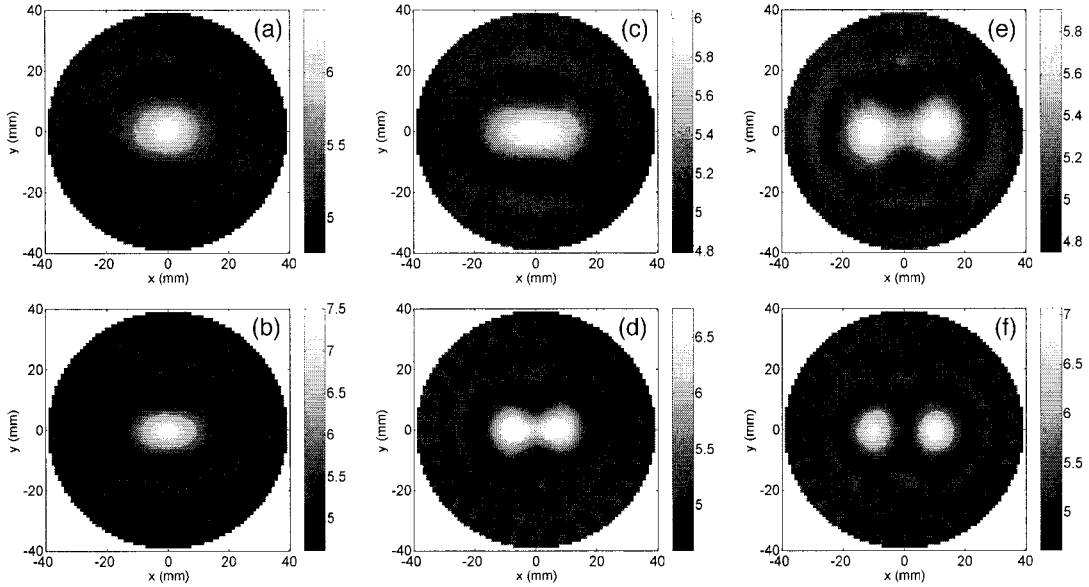

Fig. 7. Study 3: deconvolved images for two FEM meshes and three different interinclusion separation distances. (a) 717-node mesh, 10-mm center-to-center separation; (b) 1019 nodes, 10 mm; (c) 717 nodes, 14 mm; (d) 1019 nodes, 14 mm; (e) 717 nodes, 20 mm; (f) 1019 nodes, 20 mm. All inclusions have 6-mm diameter and $\mu_a^{\mathrm{incl}}/\mu_a^{\mathrm{bkgr}} = 2$. Gray-scale values are $1000 \times \mu_a$.

d [Fig. 6(b)] for a single inclusion located one-fourth of the way from the medium's center to its boundary (curves with ○ symbols) and for a single inclusion located three-fourths of the way from the center to the boundary (curves with □ symbols). The observation that the FWHMs of the reconstructed inclusion are nearly independent of d at the small-diameter end of the curves is not unexpected, because here the finite internode separation ($\overline{\Delta s} = 0.9$ mm) of the fixed 1019-node FEM mesh determines the size of the inclusion in the image. For values of d larger than $\overline{\Delta s}$, however, the FWHM values are nearly proportional to d, with a discrepancy smaller than 3 mm for both inclusion locations and all diameters.

As described in Subsection 2.D above, the simulation studies 3–6 all involved the use of a pair of finite-diameter inclusions (with the same d and the same μ_a) in a circular medium with full tomographic S–D configurations while different groups of control parameters were varied. The effect of varying the coarseness of the inverse-problem mesh while the number of S–D channels N_c is held constant was considered in study 3, which made use of 1024 S–D channels and either 717 or 1019 nodes in the inverse-problem mesh. Although it might be thought that increasing N_p would necessarily improve resolving power, it is also possible that the direct benefit derived from reducing the internode separation would be offset by increasing the degree of underdeterminedness of the inverse problem (recall that the numbers of unknowns solved for are two times N_p, or 1434 and 2038).

The reconstructed images obtained after application of the deconvolution operator are shown in Fig. 7 for both meshes and for three different interinclusion separations. [The uncorrected images are not shown for this study owing to space limitations, but in all cases the inclusions are unresolved and the appearance of the image is similar to that of Fig. 7(a).] It is seen that the two inclusions are not well resolved at their smallest separation when points on their boundaries approach to within 4 mm, which is smaller than their 6-mm diameters. The finer mesh is capable of resolving the inclusions when they are separated center to center by 14 mm, but the coarse mesh resolves them only at the largest separation modeled. Within the range of N_p values considered here, the qualitative advantage gained by decreasing $\overline{\Delta s}$ outweighs any disadvantage resulting from making the inverse problem more underdetermined.

Quantitatively, the corrected images yield global spatial correlation (r_s) values that are 35.1%, 35.9%, and 37.0% larger for $N_p = 1019$ than for $N_p = 717$, when the interinclusion separation is 10, 14, and 20 mm, respectively. Simultaneously, the RMSE (ε) is 3.6%, 1.1%, and 6.8%, respectively, lower in the fine-mesh image than in the corresponding coarse-mesh result. These trends agree with the qualitative trends seen on inspection for the 14- and 20-mm interinclusion separations, and they reveal that a comparable degree of improvement is achieved even in the 10-mm separation case [Figs. 7(a) and 7(b)], in which the difference between the coarse- and fine-mesh corrected images is not as apparent to the eye.

As a complement to the preceding case, the effect of varying the number of S–D channels with a fixed inverse-problem mesh was considered in study 4, which combined $N_c = 256$, 768, or 1024 with $N_p = 717$. Deconvolved reconstructed images are shown in Fig. 8 for each of the three values of N_c, along with an uncorrected image for the 1024-channel case. Uncorrected images for the other two cases are not

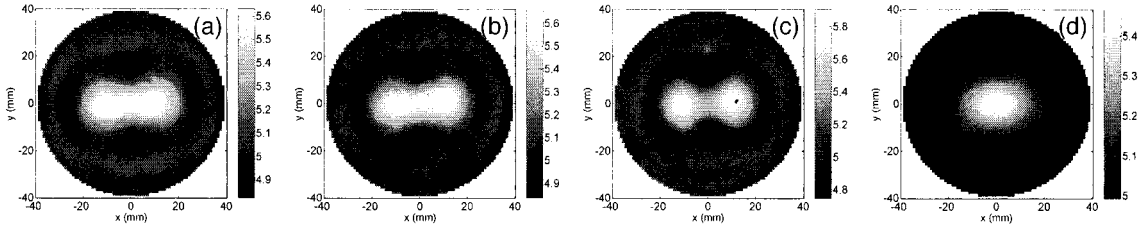

Fig. 8. Study 4: images for different numbers of S–D channels, N_c. (a)–(c) Corrected images for $N_c = 256$, 768, and 1024, respectively. (d) Uncorrected image, $N_c = 1024$. Inclusion center-to-center distance is 20 mm. A 717-node mesh was used for all reconstructions. The inclusion diameter, absorption contrast, and FEM mesh are the same as in study 3 (Fig. 7). Gray-scale values are $1000 \times \mu_a$.

shown, because, under both visual inspection and quantitative analysis, they are almost indistinguishable from the result in Fig. 8(d). (Quantitatively, the largest r_s value exceeds the smallest by 4.2%, whereas the greatest difference between ε values is only 0.2%.) Spatial deconvolution enhances the resolving power irrespective of the number of S–D channels, and the degree of improvement increases with increasing N_c. These differences between the uncorrected and the deconvolved images, which are apparent under visual inspection, are corroborated by the quantitative accuracy indices: r_s increases by 23.8%, 31.3%, and 56.2% for $N_c = 256$, 768, and 1024, respectively; the corresponding decreases in ε are 3.4%, 4.0%, and 7.3%.

These results also indicate that, although there exists a fundamental limit to the quantity of independent information that can be obtained with surface measurements,[15] that limit has not yet been reached with the largest N_c employed in this simulation experiment. However, if the image-enhancement procedure were not employed, the opposite conclusion could be easily drawn from the uncorrected images. As pointed out in Ref. 2, a question worth investigating is whether earlier assessments of the limits on image quality obtainable with linear DOT reconstruction algorithms may have been overly pessimistic.

The spatial resolution curves in Figs. 4 and 5 led us to expect that the limited resolving power seen in the coarse-mesh images of Fig. 7 is also depth dependent. To test that prediction, we conducted simulation study 5, wherein all conditions are identical to those used to generate the image shown in Fig. 7(c) (i.e., $N_c = 1024$, $N_p = 717$, 6-mm diameter inclusions separated by 14 mm center to center) except that the inclusions were translated along the Y axis, from a starting position of 0 to either 15 or 25 mm. Reconstructed images before and after spatial deconvolution are shown in Fig. 9 for each of the three inclusion positions. It is clear that the resolving power (which of course could be further improved by increasing N_p, as in Study 3) does increase with increasing distance from the center, as expected. Likewise, when the uncorrected and corrected images are compared quantitatively, the increase in r_s grows from 20.4% when $Y = 0$ to 78.1% when $Y = 25$ mm, while the decrease in ε concomitantly rises from 5.3% to 13.7%. A prac-

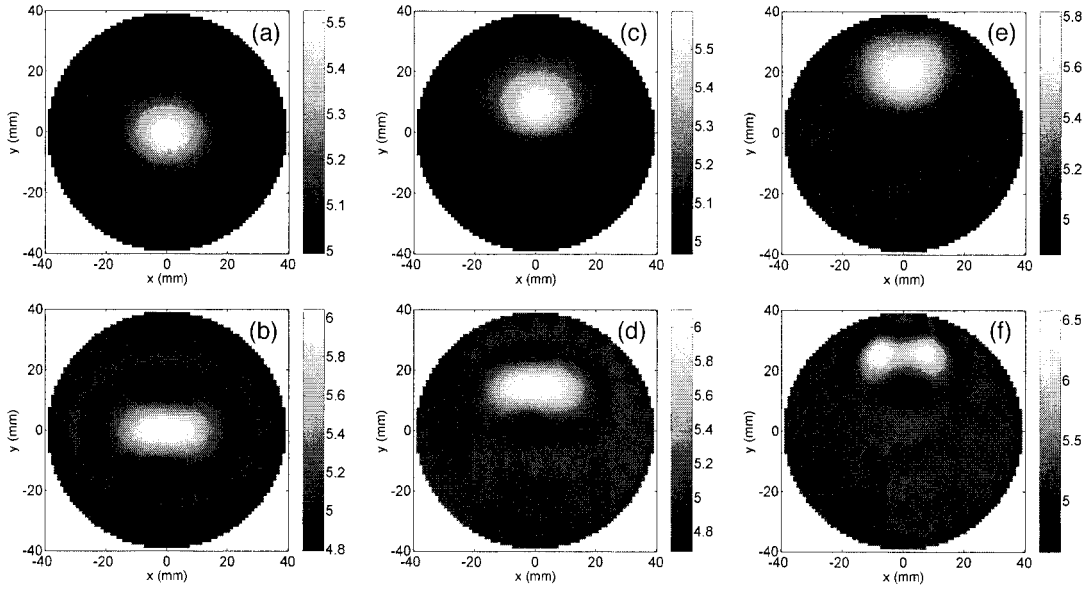

Fig. 9. Study 5: images for different inclusion depths. (a), (b) Images before and after deconvolution, with inclusions at $y = 0$. (c), (d) Inclusions at $y = 15$ mm. (e), (f) Inclusions at $y = 25$ mm. Inclusion diameter, absorption contrast, and FEM mesh are the same as in study 4 (Fig. 8), and the center-to-center distance is 14 mm. Gray-scale values are $1000 \times \mu_a$.

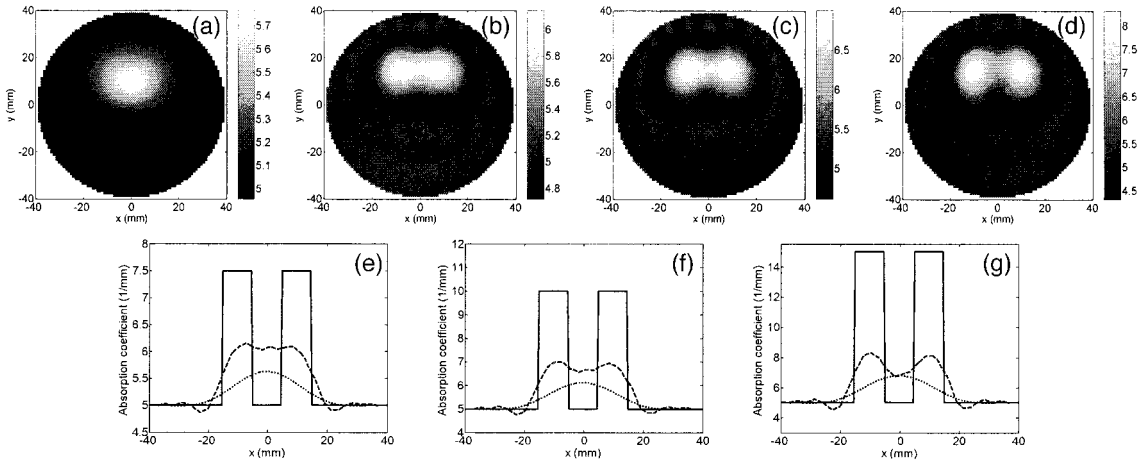

Fig. 10. Study 6: images and 1D μ_a distributions for different inclusion contrasts. (a) Uncorrected image, $\mu_a^{\mathrm{incl}}/\mu_a^{\mathrm{bkgr}} = 1.5$. (b)–(d) Corrected images, $\mu_a^{\mathrm{incl}}/\mu_a^{\mathrm{bkgr}} = 1.5$, 2, and 3, respectively. (e)–(g) μ_a distributions along $y = 15$ mm, $\mu_a^{\mathrm{incl}}/\mu_a^{\mathrm{bkgr}} = 1.5$, 2, and 3, respectively. The solid curve is ideal values; dotted and dashed curves are sections through the uncorrected and corrected images, respectively. Each inclusion diameter is 10 mm; inclusions are located at $y = 15$ mm, with center-to-center distance of 20 mm. The FEM mesh is the same as in study 5 (Fig. 9). Gray-scale [(a)–(d)] and ordinate axis [(e)–(g)] values are $1000 \times \mu_a$.

tical benefit of studies of this type is that their results could guide us in the generation of depth-dependent regularization parameters[26] that are optimized for a given medium, mesh, and S–D configuration.

The final control parameter that was included in this group of simulation experiments was the inclusion-versus-background absorption contrast. A motivating concern, as also for the subsequent systematic error study, is the possibility that the effect of using a given **F** matrix might be deleterious rather than beneficial if the target medium contains optical coefficient values well outside the range that was modeled in the computations that generated **F**. Accordingly, in study 6 the mesh, S–D configuration, and inclusion positions were all fixed while the inclusions' μ_a was varied from 1.5 to 3 times that of the background. It should be noted (see Subsection 2.A) that in the filter-generating computations, μ_a deviated from the background value by at most 2%. Deconvolved reconstructed images are shown in Fig. 10 for each of the three contrast levels, along with the uncorrected image obtained when $\mu_a^{\mathrm{incl}} = 0.0075\ \mathrm{mm}^{-1}$; uncorrected images for the other two cases are almost indistinguishable from the result in Fig. 10(a) and are not shown. It is found that the motivating conjecture is not borne out, and that the resolving power in fact improves with increasing contrast.[27,28] Additional insight into the latter observation is obtained by examining 1D transects through the recovered inclusions, which are plotted in Figs. 10(e)–10(g). The (dashed) curves corresponding to the corrected images reveal that as contrast increases the quantitative discrepancy between the target and the image grows (e.g., the absolute value of ε is about 4 times larger for $\mu_a^{\mathrm{incl}}/\mu_a^{\mathrm{bkgr}} = 3$ than for $\mu_a^{\mathrm{incl}}/\mu_a^{\mathrm{bkgr}} = 1.5$) but that the recovered μ_a in the regions corresponding to the inclusions grows more rapidly than does the recovered μ_a in the interinclusion region. Thus, in comparing the corrected with the uncorrected images, the percentage decrease in ε actually grows slightly from the lowest-contrast (17.1%) to the highest-contrast (17.6%) case, and the percentage increase in r_s concomitantly grows from 70.7% to 78.0%.

Results from study 6 have an important practical consequence; namely, they indicate that the utility of a particular deconvolution operator does not require extremely close agreement between the properties of the filter-generating and the target media. To further pursue the same issue, we conducted study 7, in which mismatch between both μ_a and μ_s' of the target medium and filter-generating medium was modeled. (See Subsection 2.B and Tables 2–3 for details.) In these computations all target media contained four 6-mm diameter inclusions embedded in a 80-mm-diameter background medium. The inclusions were located at the corners of a square, with a minimum center-to-center separation of 21 mm, and in all cases the inclusion-background absorption contrast was exactly 2. The resulting set of 56 deconvolved reconstructed images (8 values for target μ_a, 7 values for target μ_s') are shown in Fig. 11. The single case for which the optical coefficients of the filter-generating medium match those of the target medium is indicated by means of a square drawn around the image. The uncorrected image for this case is also shown below the matrix of corrected images; the remaining 55 are all qualitatively similar to this one. The corresponding values for the percentage increase in r_s and the percentage decrease in ε (comparing corrected and uncorrected images) for selected deconvolved images are given in Table 4. Inspection of Fig. 11 reveals that the single image-enhancing filter used had beneficial effects in a significant percentage of cases. These results run in a broad swath from the lower left to the upper right of Fig. 11 and include cases wherein there is appreciable mismatch in both μ_a and μ_s'. In a finding complementary to that of study 6, the quantitative index data in Table 4 reveal

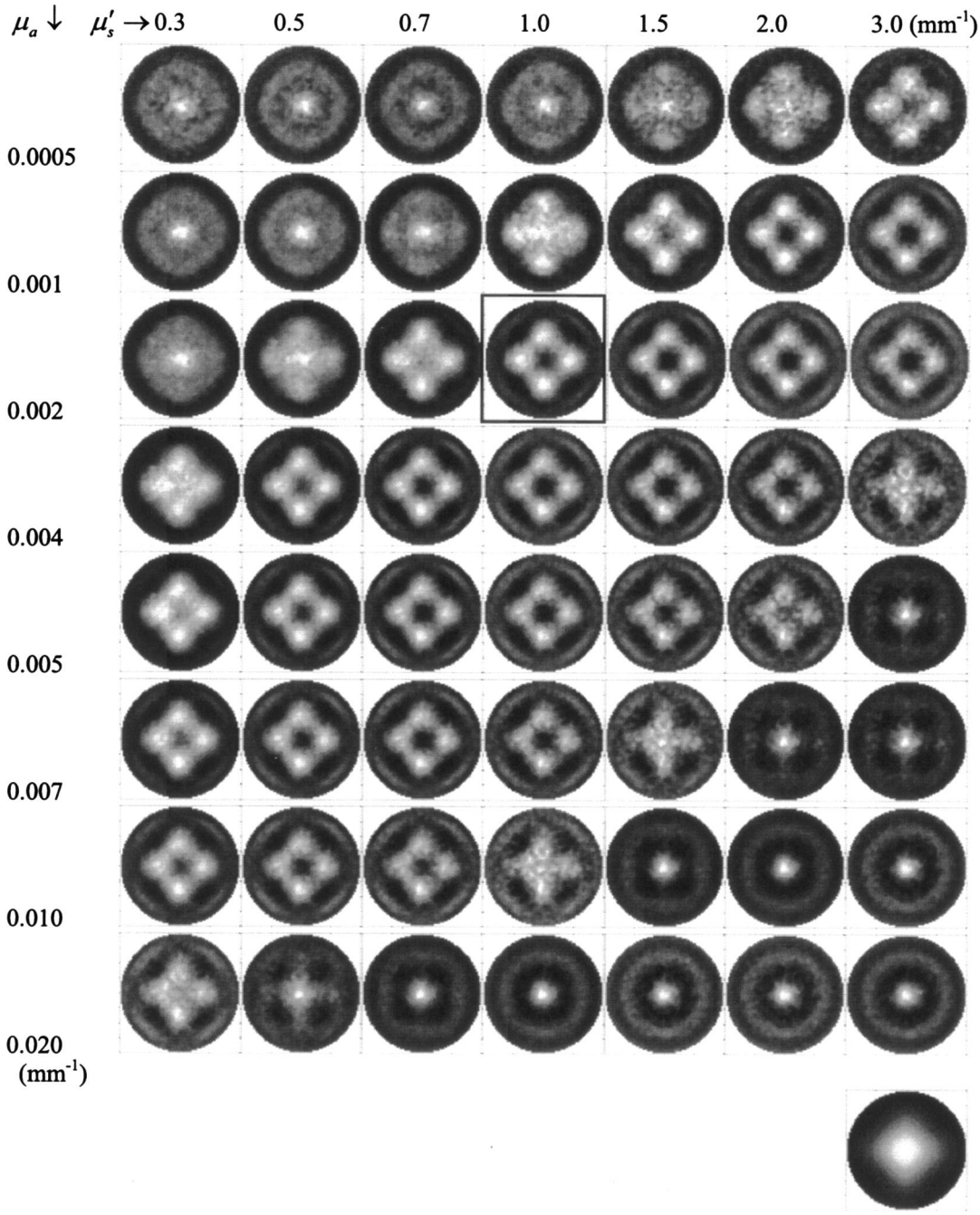

Fig. 11. Study 7: application of a filter generated for a medium with one set of optical coefficients to target media with different background properties. The filter-generating medium had $\mu_a = 0.002\ \text{mm}^{-1}$ and $\mu_s' = 1.0\ \text{mm}^{-1}$. For the 56 test media, the background μ_a and μ_s' ranges were 0.0005–0.02 and 0.3–3.0 mm^{-1}, respectively. Also shown is the uncorrected image for the target medium with $\mu_a = 0.002\ \text{mm}^{-1}$ and $\mu_s' = 1.0\ \text{mm}^{-1}$; the remaining 55 are qualitatively similar. In every case μ_s' was spatially homogeneous and $\mu_a^{\text{incl}}/\mu_a^{\text{bkgr}} = 2$.

that for some combinations of target medium properties the percentage increase in r_s and percentage decrease in ε are larger than those obtained for the perfect-match case. It can reasonably be concluded that the method presented here and in Refs. 1 and 2 is sufficiently robust to incomplete knowledge of the target medium's average optical coefficients that it could be applied to laboratory or clinical data, and that the library of $\mathbf{F}$ matrices needed to handle the expected range of medium properties need not be prohibitively large.

The final simulation experiment that made use of a full tomographic S–D configuration (study 8) was conducted to compare the effects of the linear spatial deconvolution technique with an iterative Newton–Raphson reconstruction algorithm. As explained in Refs. 1 and 2, the two approaches proceed from different conceptual premises regarding the origin of the

Table 4. Quantitative Accuracy Indices for Study 7 (Systematic Error Study)

Background μ_s'	Background μ_a (mm^{-1})	Increase of r_s (%)	Decrease of ε (%)
1.0[a]	0.002[a]	60.4	4.6
1.0	0.001	50.4	4.3
1.0	0.004	73.9	6.4
0.7	0.002	34.9	2.2
1.5	0.002	71.2	6.1
3.0	0.0005	39.7	2.9
0.7[b]	0.01[b]	87.6	0.0
0.5[c]	0.01[c]	83.9	7.1

[a]The case for which the filter-generating and target media have identical background properties.
[b]This target medium, out of all considered, yields the greatest percentage increase of r_s.
[c]This target medium, out of all considered, yields the greatest percentage decrease of ε.

errors typically found in images obtained by use of linear perturbation methods. The Newton–Raphson approach is based on the assumption that the effects result primarily from an inability of equations with the form of Eqs. (4) and (5) to represent the true relationship between medium properties and detector data. The linear spatial deconvolution technique assumes that the most important source of error is the information-spread phenomenon described in Subsection 2.A. The target medium used for the comparison study was an 86-mm-diameter circular disk with an inclusion consisting of a 20-mm-diameter circular region of elevated absorption (see Tables 2 and 3 for other defining properties). The goal was to achieve as close a match as possible to the test-medium properties used in Ref. 12. The images we have reconstructed before and after deconvolution and with and without the presence of multiplicative noise in the forward-problem solutions are shown in Fig. 12. Quantitative comparisons of the recovered locations, diameters, and peak μ_a values of the inclusion between the two methods are given in Table 5. The gray-scale maps and 1D transects in Fig. 12 demonstrate that, as in the preceding studies involving smaller-diameter inclusions, the uncorrected image exhibits location bias and shape distortion and that the deconvolution method substantially corrects these errors. A trade-off is that, at the same time, noise artifacts are amplified. Techniques for reducing the effect of noise are available and would be used in practice. Naturally, use of these techniques (and likewise for the ringing-artifact reduction algorithms referenced earlier) would be likely to bring into play an additional trade-off; namely, that they would to some degree negate the improvement in spatial resolution that the deconvolution achieves.

Table 5. Accuracy of Recovered Inclusion Properties for Study 8 and Ref. 12

Medium or Image	FWHM (mm)	Depth (mm)	μ_a Peak Value (1/mm)
Target medium	20.0	25.0	0.0200
Ref. 12 image	24.0	24.0	0.0215
Study 8 image	24.2	24.1	0.0146

Many of the important prospective applications of DOT, such as functional neuroimaging,[8] do not permit the use of fully tomographic arrangements of

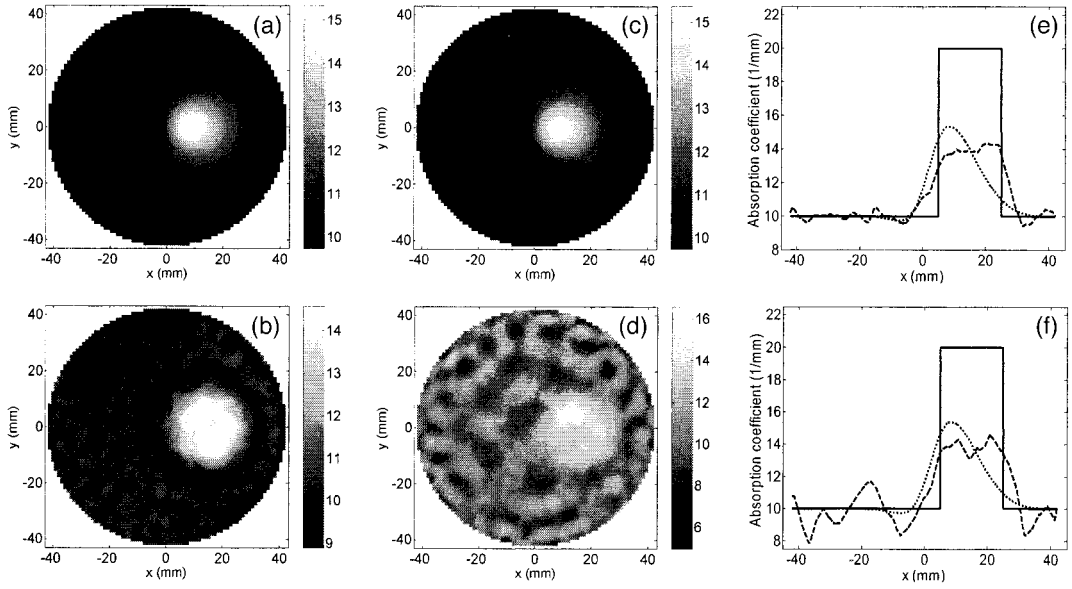

Fig. 12. Study 8: images and 1D sections for a 20-mm-diameter inclusion with and without multiplicative noise in detector data. (a), (b) Uncorrected and corrected images from noise-free data. (c), (d) Images from noisy data. (e), (f) 1D sections along $y = 0$ for noise-free and noisy cases, respectively. Solid curves are ideal profiles; dotted and dashed curves are uncorrected and corrected results, respectively. The inclusion is centered at (15, 0) mm, $\mu_a^{\text{incl}}/\mu_a^{\text{bkgr}} = 2$. The reconstruction mesh had 1019 nodes. Gray-scale [(a)–(d)] and ordinate axis [(e), (f)] values are $1000 \times \mu_a$.

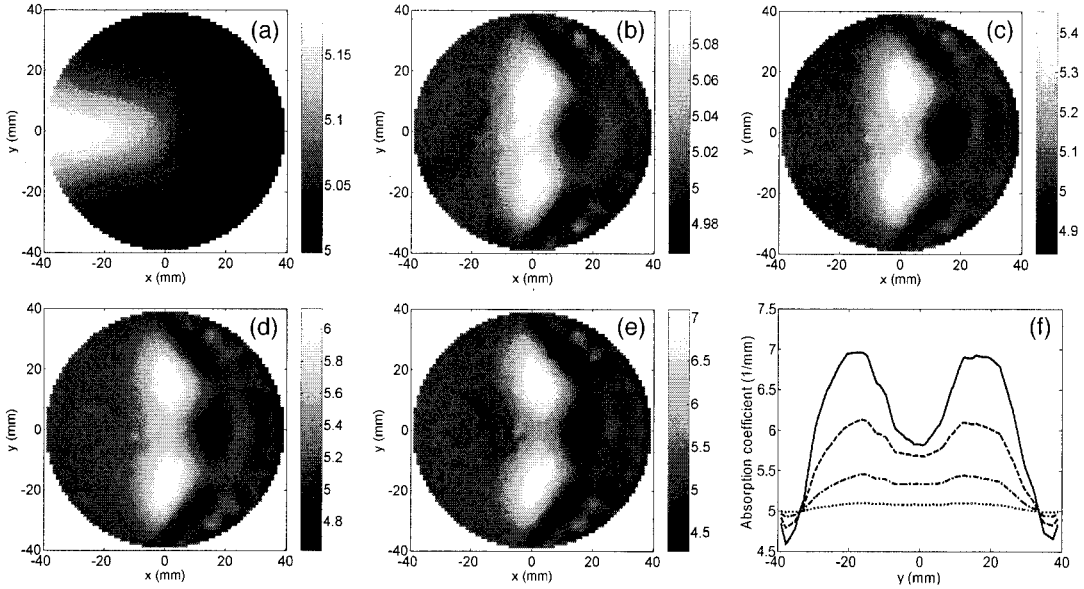

Fig. 13. Study 9: images and corresponding 1D sections with a two-inclusion target medium for different inclusion-background contrasts and the limited-view S–D configurations shown in Fig. 2(b). (a) Uncorrected image, $\mu_a^{\text{incl}}/\mu_a^{\text{bkgr}} = 1.2$. (b)–(e) Deconvolved images, $\mu_a^{\text{incl}}/\mu_a^{\text{bkgr}} = 1.2$, 2, 4, and 8, respectively. (f) 1D sections along $x = 0$ through images in (b)–(e), for $\mu_a^{\text{incl}}/\mu_a^{\text{bkgr}} = 1.2$ (dotted curve), 2 (dashed–dotted curve), 4 (dashed curve), and 8 (solid curve). The 6-mm-diameter inclusions are located at (0, 15) and (0, 15). The reconstruction mesh had 717 nodes. Gray-scale [(a)–(e)] and ordinate axis [(f)] values are $1000 \times \mu_a$.

sources and detectors. Although Refs. 1 and 2 included demonstrations of the effectiveness of the image-enhancing algorithm in limited-view contexts, its sensitivity to imperfect matches between the properties of target and filter-generating media was not extensively studied. To begin to address this, we conducted study 9, which was analogous to study 6—fixed FEM mesh, S–D configuration and inclusion positions, and variable inclusion-versus-background absorption contrast—but employed the 216-channel S–D configuration shown in Fig. 2(b). [See Table 3, and Fig. 14(e) below, for the sizes and locations of inclusions.] Four sets of detector readings were generated, for inclusion μ_a levels of 0.006, 0.01, 0.02, and 0.04 mm^{-1}, while the background μ_a was fixed at 0.005 mm^{-1}. Enhanced reconstructed images are shown in Fig. 13 for each of the four contrast levels, along with an uncorrected image for $\mu_a^{\text{incl}} = 0.006\ \text{mm}^{-1}$; uncorrected images for the other three cases are almost indistinguishable from the result in Fig. 13(a) and are not shown. Here it is seen that, unlike the full tomographic examples, the structure of the inclusions is not even approximately revealed in the uncorrected image. Instead, the medium's μ_a is apparently recovered in the region of lowest weight, in the half of the medium opposite the sources and detectors. However, the spatial image-correction operation produces results whose accuracy is comparable with that seen in the preceding examples. Also, as in study 6, it is seen here that the resolving power improves with increasing contrast. The 1D transects through the recovered inclusions, plotted in Fig. 13(f), show that the underlying phenomenology is the same for images derived from limited-view data as it is in the full tomographic case. Namely, the quantitative discrepancy between the target and the image grows (e.g., the absolute value of ε is ~35 times larger for $\mu_a^{\text{incl}}/\mu_a^{\text{bkgr}} = 8$ than for $\mu_a^{\text{incl}}/\mu_a^{\text{bkgr}} = 1.2$) as absorption contrast increases, but the recovered μ_a in the regions corresponding to the inclusions grows more rapidly than does the recovered μ_a in the interinclusion region. Taken together, these results reinforce the suggestion that the spatial deconvolution method will likely be applicable in laboratory and clinical imaging studies.

Examination of the large discrepancy between the target medium and the uncorrected image in Fig. 13(a) suggested the question of whether an iterative reconstruction algorithm could be successfully applied in such a case and, if so, how the final result would compare with that obtained by using the spatial filtering technique. In study 10 the two approaches were directly compared for the same limited-view S–D geometry as used in study 9 [Fig. 2(b)], and the two target media shown in Figs. 14(a) and 14(e). For this study the forward- and inverse-problem algorithms described in Subsections 2.C and 2.D were applied, in alternating fashion, to iteratively update the reconstructed image. We used an error-based convergence criterion, terminating when the detector data errors were lower by a factor of 10^{-3} than after the first iteration. In practice, approximately 50 iterations were required. Shown in Fig. 14 are the uncorrected images of the target media [Figs. 14(b) and 14(f)], the enhanced images produced by applying the appropriate spatial deconvolution operator [Figs. 14(c) and 14(g)], and the images after the 50th iterative update [Figs. 14(d) and 14(h)]. Intersecting gridlines that indicate the locations of the inclusions in the target media are included in Figs.

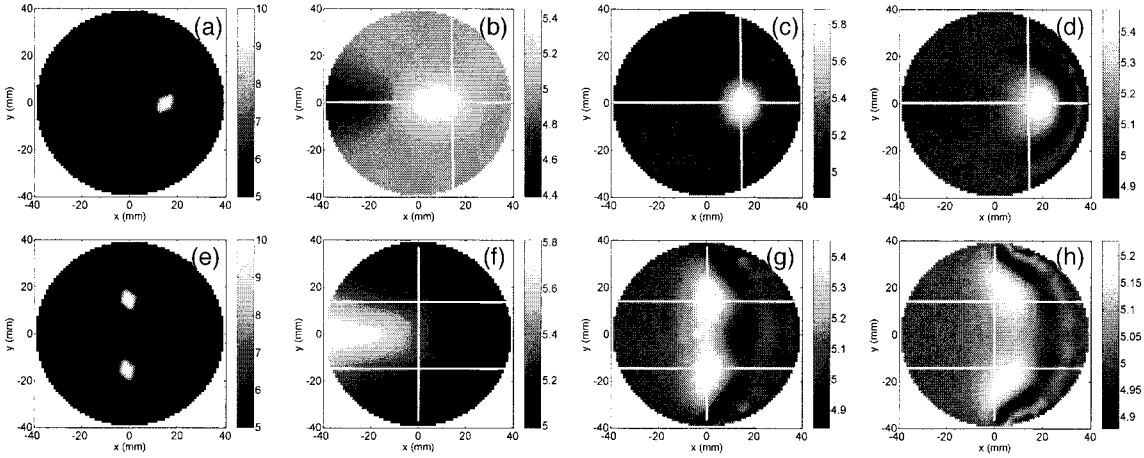

Fig. 14. Study 10: images produced by spatial deconvolution and by a LM method, for the limited-view S–D configurations shown in Fig. 2(b). (a)–(d) One-inclusion target, uncorrected image, deconvolved image, and image produced by 50 LM iterations, respectively. (e)–(h) The same as in (a)–(d), but for a two-inclusion target. The inclusion diameter and FEM mesh are the same as in study 9 (Fig. 13), and $\mu_a^{\text{incl}}/\mu_a^{\text{bkgr}} = 2$. Gray-scale values are $1000 \times \mu_a$.

14(b)–14(d) and 14(f)–14(h). It is clear from these results that the linear (deconvolution) method produces qualitatively superior results, in which the maxima of the recovered inclusions are at their correct locations. The nonlinear (iterative) algorithm used here, on the other hand, biases their locations toward the sources and detectors.

In this and the preceding simulation experiment, the uncorrected images have such low values for r_s and ε that computation of the percentage change between them and the corrected images cannot meaningfully be carried out. Here, however, the difference between the accuracy of the images produced by the linear and nonlinear approaches can be quantified in several ways. In the one-inclusion case, the spatial correlation r_s between image and target media is 47.8% larger for Fig. 14(c) than for Fig. 14(d), and the RMSE ε is 6.3% lower in Fig. 14(c) than in Fig. 14(d). Also, the absolute location errors for the recovered inclusion are $E_X = 0.35$ mm, $E_Y = 0.15$ mm in Fig. 14(c) and $E_X = 2.6$ mm, $E_Y = 0.25$ mm in Fig. 14(d). In the two-inclusion case, r_s for Fig. 14(g) is 89.5% larger than that for Fig. 14(h), and ε is 3.7% lower in Fig. 14(g) than in Fig. 14(h). The recovered inclusions' absolute location errors are $E_{X1} = 1.2$ mm, $E_{Y1} = 0.25$ mm and $E_{X2} = 1.0$ mm, $E_{Y2} = 0.20$ mm in Fig. 14(g); and $E_{X1} = 6.2$ mm, $E_{Y1} = 4.3$ mm and $E_{X2} = 6.0$ mm, $E_{Y2} = 4.5$ mm in Fig. 14(h).

The disk-shaped media used in all the preceding experiments is an adequate model for many DOT applications. Many others, however, cannot be modeled well this way but call for a slab-shaped medium, either because the tissue structure itself approximates a slab or because compression of the tissue causes it to assume that geometry. Consequently, in the final two simulation experiments (studies 11 and 12) the filter-generating and target media were rectangular. The backreflection S–D configuration sketched in Fig. 2(c) was modeled in study 11, while the control parameter was the location of the inclusion along the Y axis. For the inclusions located closest to and farthest from the sources and detectors, the target media and the reconstructed images, before and after application of the image-enhancement algorithm, are shown in Fig. 15. The corresponding 1D sections through the target media and images are plotted for all four inclusion locations in Fig. 16.

Consistent with preceding spatial resolution versus location results, the sizes and shapes of the recovered inclusions become increasingly accurate as the inclusion depth decreases. It is also seen that the uncorrected images exhibit a tendency, analogous to that in the limited-view circular medium cases, for spatial skewing of the recovered μ_a into the direction of the lowest-weight region of the slab. In every case the spatial deconvolution technique improves the image accuracy with respect to inclusion location, size, and shape, but unsurprisingly the final image becomes less accurate with increasing inclusion depth. Likewise, the quantitative error in the peak recovered μ_a value increases with depth, with a nearly ideal reconstruction achieved for the most superficial inclusion. As inspection of Fig. 16 would lead one to expect, the percentage decrease in ε resulting from use of the image-enhancement method falls monotonically with increasing depth, from 51.3% for the most superficial inclusion to 6.7% for the deepest. However, Fig. 16 also suggests that the percentage increase in r_s will not be a monotonic function of depth. This expectation is borne out quantitatively, as r_s increases by 45.1% for the inclusion located at $Y = 20$ mm, by 161% when $Y = 10$ mm, and by 205% when $Y = 0$, but it then falls to 116% when $Y = -10$ mm. Future studies involving media more than 60 mm thick may be undertaken to determine whether this trend is principally a depth effect or principally a boundary layer effect.

Study 12 was another limited-view simulation experiment that made use of the rectangular medium

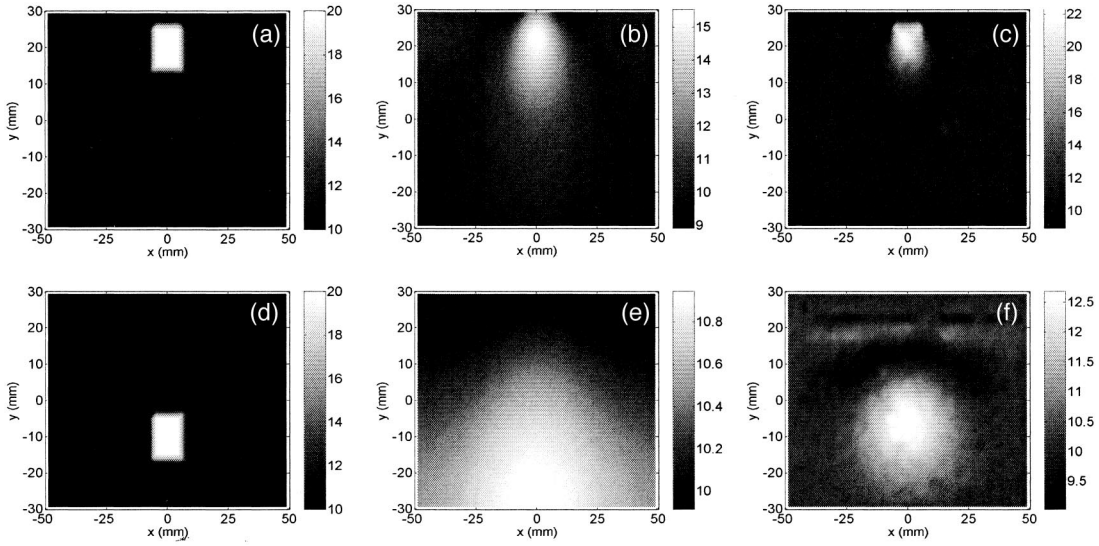

Fig. 15. Study 11: images of rectangular target media, using the limited view (backreflection) S–D configurations shown in Fig. 2(c). (a)–(c) Target with inclusion located at (0, 20) mm, the uncorrected image, and the deconvolved image, respectively. (d)–(f) Target with inclusion at (0, −10) mm, the uncorrected image, and the deconvolved image, respectively. The inclusion area is $10 \times 10\ \mathrm{mm}^2$, $\mu_a^{\mathrm{incl}}/\mu_a^{\mathrm{bkgr}} = 2$. The reconstruction mesh had 1025 nodes. Gray-scale values are $1000 \times \mu_a$.

geometry. This was complementary to the preceding study in that the sources and detectors were on opposite edges, modeling a single-view transmission measurement (such as a DOT mammography application in which the tissue is compressed between flat plates[29]). With this S–D configuration the quality of the reconstructed images would not be as strongly depth dependent as in study 11; accordingly, the inclusion used here was a single FEM mesh node located at the medium's geometric center. The control parameter was the number of sources and detectors, which was varied from 9 ($N_c = 81$ total S–D channels) to 33 ($N_c = 1089$ channels) of each. Because the width of the medium (100 mm) and the inverse-problem mesh ($N_p = 1025$ nodes) are fixed, increasing the number of sources and detectors necessarily also increases their spatial density and changes the character of the inverse problem from strongly underdetermined to slightly overdetermined.

The structure of the target medium, the uncorrected reconstructed image for the 81-channel case (the other two uncorrected images are nearly indistinguishable and are not shown), and the corrected images for all three cases are shown in Fig. 17. The corresponding 1D sections through the images are plotted in Fig. 18. Here the spatial deconvolution method achieves a degree of reduction in the size of the recovered inclusion that is greater than that seen in the preceding experiments—the smallest percentage increase in r_s, going from the uncorrected to the corrected images in Fig. 17, is 139%. Evidently this is because the spatial resolution of the uncorrected im-

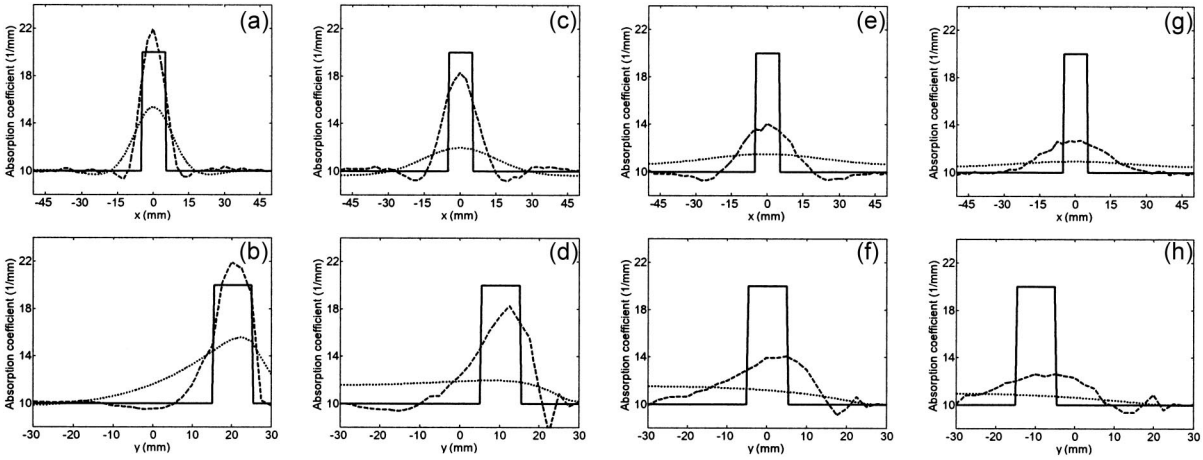

Fig. 16. Study 11: 1D sections through images in Fig. 15, for four inclusion locations. (a) Section along the line $y = 20$ mm, inclusion centered at (0, 20) mm; (b) $x = 0$, (0, 20) mm; (c) $y = 10$, (0, 10) mm; (d) $x = 0$, (0, 10) mm; (e) $y = 0$, (0, 0) mm; (f) $x = 0$, (0, 0); (g) $y = -10$, (0, −10) mm; (h) $x = 0$, (0, −10) mm. The solid curve is ideal values; dotted and dashed curves are sections through the uncorrected and corrected images, respectively. Ordinate axis values are $1000 \times \mu_a$.

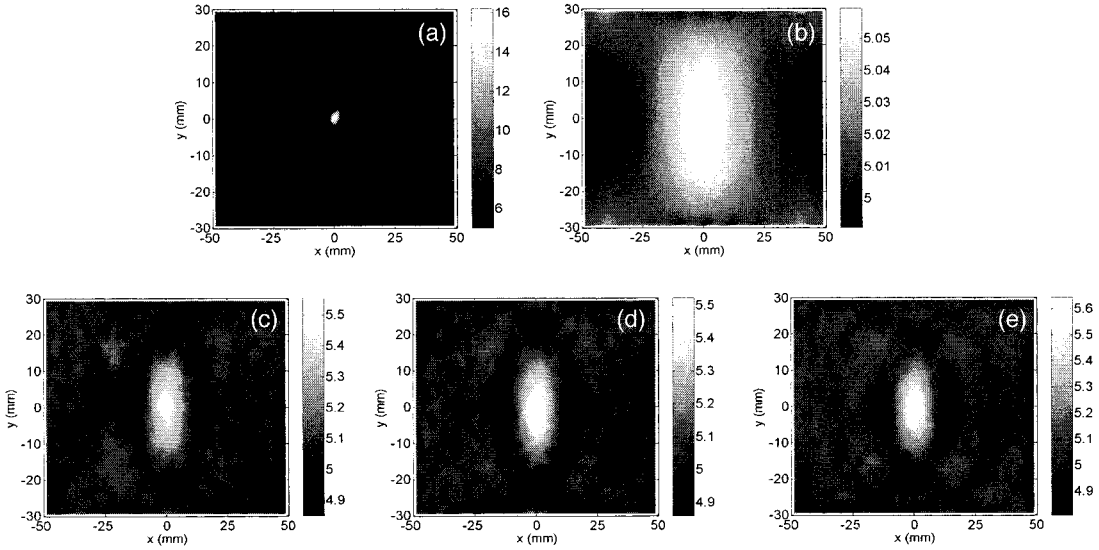

Fig. 17. Study 12: images of rectangular target media, using the limited-view (transmission) S–D configuration shown in Fig. 2(d). (a) Target with one point-like inclusion located at (0, 0). (b) Uncorrected image, $N_c = 81$. (c)–(e) Deconvolved images, $N_c = 81$, 289, and 1089, respectively. The FEM mesh is the same as that in study 11 (Fig. 15). Gray-scale values are $1000 \times \mu_a$.

ages is, not surprisingly, worse for a single-view transmission measurement than for the other S–D configurations that were considered here. A close examination of the plots in Fig. 18 reveals that the spatial resolution of the corrected image does improve slightly as N_c increases. The effect is small, however, which is likely attributable partly to the existence of a fundamental resolution limit[15] and partly to the fixed finite internode separation of the mesh used for the inverse-problem computations. (Future studies involving variable mesh coarseness may be undertaken to determine the relative importance of each effect.) More striking and possibly of more practical importance, however, is the reduction in the amplitude of the numerical error artifacts with increasing N_c. This suggests that increasing the number of channels could be beneficial even in cases in which theoretical considerations imply that doing so does not increase the information content of the measurement.

4. Discussion

In previous reports we have described a numerical approach for improving the quality of DOT reconstructed images via a linear spatial deconvolution process and have presented preliminary results dem-

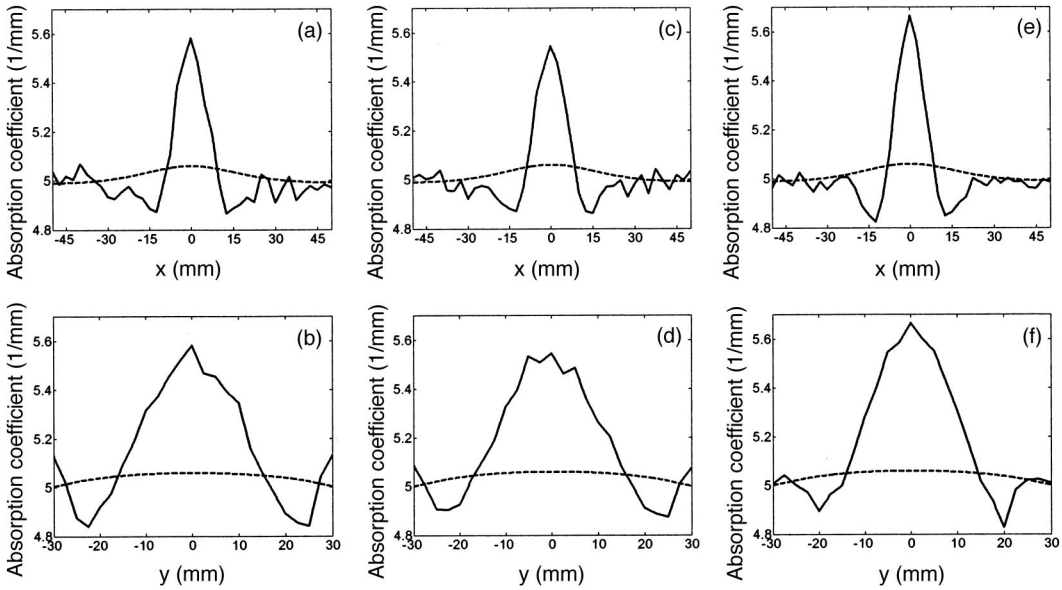

Fig. 18. Study 12: 1D sections through images shown in Fig. 17. (a), (b) Distributions along $y = 0$ and $x = 0$, $N_c = 81$. (c), (d) $N_c = 289$. (e), (f) $N_c = 1089$. Dashed and solid curves are sections through the uncorrected and corrected images, respectively. Ordinate axis values are $1000 \times \mu_a$.

onstrating the method's efficacy.[1,2] The test cases reported earlier, and in the present paper, involve the use of linear perturbation methods for computing solutions to the DOT inverse problem; it is widely believed that these algorithms produce images that exhibit low spatial resolution and only modest accuracy in object location. An important implication of the current line of research is that these properties are not intrinsic to the linear image reconstruction strategy. Rather, in many cases the image does contain accurate information regarding the optical coefficients of the target medium, but in a spatially distorted form.

The purpose of this paper has been to report simulation studies meant to characterize in detail the improvement in image quality that is achieved by use of the deconvolution procedure. The primary goal was to ascertain the limits of spatial resolution and of qualitative (i.e., positions, shapes, and sizes of inclusions) and quantitative (i.e., magnitude of recovered absorption and scattering coefficients) accuracy that can be achieved by this method. The second goal was to explore the method's sensitivity to differences between the properties of the media used to generate a deconvolution operator and of the medium to which that operator is subsequently applied.

A. Significance and Implications of the Results

1. Location Error

In several simulation studies, the location error for a point inclusion was explicitly computed. As described above, when location error for uncorrected images was plotted against distance from the medium's center, a biphasic trend was observed for the error in the dimension parallel to the inclusion's displacement from the center (E_X in Figs. 4 and 5, or E_r, for radial error, more generally), but the location error in the perpendicular dimension (E_Y in Figs. 4 and 5, or E_θ, for angular error, more generally) exhibited no clear dependence on displacement. Moreover, for most inclusion locations the former location error was larger than the latter by an order of magnitude. Deconvolution leaves the qualitative shapes of the error-versus-displacement curves largely unchanged, but it reduces the magnitudes of E_X and E_Y by a factor of 5–7. The possibility has been raised to us that the tendency toward large radial errors in the uncorrected images is caused by some aspect of the reconstruction algorithm itself, such as the scaling of weight matrix ($\mathbf{W}$) columns to uniform sums.[30] However, any suggestion that use of column scaling should therefore simply be abandoned could not be adopted, because of the vital function that scaling performs by reducing the condition number of $\mathbf{W}$. That is, even if it were conclusively shown that the algorithm outlined in Subsection 2.D causes the location errors seen in study 1, the algorithm has a practical benefit that outweighs any potential liability resulting from the errors. The two-step strategy used here and in the previous reports, of first reconstructing an image and then performing an *a posteriori* correction, leads to a final result that is superior to that which would be obtained by, say, abandoning the step of scaling the columns of $\mathbf{W}$.

A point that cannot be definitively resolved on the basis of only the studies reported here concerns the observation that, for the particular combination of diameter and scattering coefficient used in these computations, the peak in the E_X-versus-X curve occurs when the displacement is halfway from the center to the boundary. The interpretation we have tentatively adopted is that E_X initially increases with X as a consequence of a (possibly algorithm-dependent) predictable tendency of DOT image reconstruction methods to displace all recovered optical coefficients in the direction of the lowest-weight region of the medium, and that the presence of a boundary layer is responsible for E_X reaching a maximum and subsequently decreasing. If this is correct, then one would predict that a medium having significantly larger optical thickness than that used here would have an asymmetric E_X-versus-X curve, with the maximum lying closer to the boundary than to the center.

The physical mechanism most responsible for the boundary layer has been previously elucidated.[31] Namely, for superficial locations there are large differences between weight-matrix elements associated with adjacent S–D channels, and the relative magnitudes of these differences fall rapidly with increasing depth. Consequently, there is a depth beyond which movement of the recovered optical coefficient toward the center of the medium has the effect of reducing its effect on all S–D channels, but above that depth the effect of such motion is less uniform. In the latter case, an inward displacement of an inclusion will reduce its effect on some channels but increase its effect on others. This offsetting of effects produces a reduction in magnitude of E_X for values of X sufficiently close to the boundary. That is, proximity to the sources and detectors, and not to an actual physical boundary, is the most important determinant of the boundary layer effect that is seen in the studies in which inclusion depth was varied.

2. Spatial Resolution

Reasoning analogous to that above also pertains to the spatial resolution (FWHM) and resolving power results. A difference between the spatial resolution and the location error results is that, in contrast to the latter, for the former we find no systematic difference, in terms of either functional form or magnitude, between the FWHM_X-versus-X and FWHM_Y-versus-X curves. Our consistent observation has been that the weight gradient in the radial or depth direction does not have the same effect on the resolution of the recovered location information as it seemingly has on its accuracy, for either corrected or uncorrected images. The absence of a radial weight-gradient effect also is demonstrated by the fact that the resolution is essentially independent of the inclusion's X coordinate for all positions deeper than the boundary layer.

The preceding considerations imply that some

other mechanism is responsible for the spatial resolution being poorer than the limiting value imposed by the internode separation (i.e., pixel size) of the inverse-problem mesh. Notably, the image reconstruction algorithm used here did not explicitly incorporate features to which loss of resolution typically is attributed, for example, first-order Tikhonov regularization,[17] spatial low-pass filtering, or truncating the singular-value decomposition of **W**. Rather, the greater area of the recovered inclusion relative to the one present in the target medium apparently is a reflection of the reduced sensitivity of the measured data to small location differences of deep-lying objects. This interpretation is supported by the results of study 11, in which the spatial resolution worsens with increasing inclusion depth. At its most superficial location, well inside the boundary layer, the lateral weight differences between adjacent S–D channels are large, and the uncertainty in the inclusion's position is correspondingly small. At greater depth, the area wherein the inclusion could lie and still produce a forward-problem solution that is essentially the same as (i.e., differing by less than the reconstruction algorithm's error tolerance) that obtained from the true target medium is much larger, and the image spatial resolution is correspondingly poorer.

In study 1 use of the image-enhancement procedure was found to improve spatial resolution by a factor of 1.6 to 2. Although not as large as the improvement factor for spatial location accuracy, it should be borne in mind that the finite pixel size of the inverse-problem mesh places more restrictive limits on the former parameter than on the latter. The fact that considerable improvement was obtained in all simulation experiments lends additional support to the argument put forward above, regarding the desirability and practicability of employing a two-stage (reconstruct, then enhance) strategy to produce the final image.

3. Global Accuracy Measures

When the effect of spatial deconvolution is assessed by calculating the percentage increase in spatial correlation (r_s) between image and target media, it is found that the corrected images have r_s values that are at least 20%, and in some cases well over 100%, larger than the uncorrected ones. On the other hand, comparisons of the RMSE (ε, which is a measure of the quantitative accuracy of the recovered optical coefficients, averaged over the entire area of the medium) show that this parameter invariably decreases, but by a smaller percentage—1% to 51%, and in most cases by less than 20%—than the corresponding increase in r_s. Caution must be exercised in interpreting the latter observation, for the data analyses reported here did not explore a hypothesis suggested by the preceding discussion of spatial resolution; namely, that the underestimation of maximum inclusion magnitudes, as in Figs. 10(e)–10(g), 12(e) and 12(f), 13(f), and 16, is a corollary of the overestimation of their area. Future research may make use of a more sophisticated calculation comparing, between the target medium and the image, the optical coefficient values integrated over the areas identified as inclusion and as background.

Qualitatively, the global effects of using the image-enhancement procedure do not depend on medium geometry or on the arrangement of sources and detectors on its surface. There was not a single case studied in which r_s did not increase or in which ε did not decrease. In quantitative terms, the magnitude of the improvement in spatial resolution that is achieved via spatial deconvolution is considerably higher for some S–D configurations than for others. Inspection of the results shown in the figures indicates that the principal reason for this dependence is not that the corrected images are notably more accurate in some cases than in others, but rather that the uncorrected ones are notably less so.

The spatial resolution of the uncorrected images for the case of single-view transmission geometry (study 12), for example, is notably poor. (Better-quality images have of course been obtained in the same geometry by other groups.[29] A shared characteristic of the algorithms used by these groups is higher computational overhead than the one we have adopted so that they would not be practical in time-series imaging applications of the sort that we conduct.[32]) That result could have practical consequences for clinical DOT, because this type of measurement has been suggested for use in optical mammography applications.[4] There are several factors that apparently favor the use of a single-view transmission measurement geometry: it permits certain data analysis simplifications[29,33]; it bears a close physical resemblance to an x-ray mammography measurement, even permitting consideration of a simultaneous dual-mode measurement[34]; and it is straightforward to perform the measurement while compressing the tissue, which lessens the optical thickness through which the near-infrared radiation must penetrate. However, the resulting images could be, as suggested by Figs. 17(b) and 18, too highly spatially convolved to permit the extraction of useful information if a correction such as that discussed in Subsection 2.A is not used. Also worth considering is whether the use of the technique we present in combination with feature-enhancing algorithms that have been reported by others[33] could improve the sensitivity and specificity of the latter.

4. Image Artifacts

An issue that affects the practical utility of the image-correction scheme described here is that, at the same time that the corrected images are better than their uncorrected counterparts in terms of location accuracy and spatial resolution, most of them are also significantly less smooth. That is, ringing artifacts, noise artifacts, and numerical error artifacts [e.g., the appearance of noise-like structures in cases in which the forward-problem solutions were noise-free, such as in Fig. 12(b)] are all amplified in the deconvolved images. These phenom-

ena are analogous to the artifacts seen in x-ray computed tomography images reconstructed by using a backprojection-filtering algorithm[35]; in both cases the issue is that an operation designed to correct for one particular source of error has a magnifying effect on other sources. As alluded to above, techniques for suppressing the various artifact types can be introduced, but doing so probably would partially offset the improvement in spatial resolution that deconvolution accomplishes. A goal of future research may be to seek an optimal balance between minimizing artifact amplitudes on the one hand and achieving improved spatial resolution and location accuracy on the other. Seemingly (see Fig. 18), one way of reducing artifact amplitudes could be to increase N_c, even if in theory doing so does not contribute additional independent information to the measurement. However, it must be seen if the effect observed in study 12 holds also in cases in which the measurement data contain noise and other sources of error.

5. Computational Strategies

Two of the studies have made direct comparisons between the action of the linear image-enhancement technique and that of a recursive iterative (i.e., nonlinear) reconstruction algorithm. In these it was found that, depending on the details of the latter method, deconvolution produced images either appreciably more accurate or only slightly less accurate than the nonlinear strategy. A similar observation was reported in Ref. 2 for a 3D simulation experiment; the significance of the results were discussed at length in Ref. 2 and are summarized above in Section 3. A point that does bear repetition here is that an effort aimed at developing a hybrid reconstruction strategy is clearly called for. The idea is that convergence of the iterative algorithm may be greatly accelerated by spatially deconvolving the reconstructed image after each iteration, and that reduction of artifact amplitudes may be one of the practical benefits of using a nonlinear algorithm.

As alluded to above, a concern that attended the initial demonstrations of the capabilities of this paper's image-enhancement technique was that the corrective effects might occur only if there were a nearly perfect match between the optical coefficients of the target medium's background and the corresponding temporally averaged coefficient values of the filter-generating medium. The systematic error study performed for this paper shows that in fact a considerable range of disagreement between the parameter values of the two media can be tolerated. That result encourages us to pursue the method and to test it for experimental and clinical utility.

B. Theoretical and Numerical Considerations

1. Factors Affecting the Performance of the Image-Correction Method

The mathematical development of the deconvolution algorithm, as outlined in Subsection 2.A, simply calls for the insertion of *some* training set $\mathbf{Y}$ and the corresponding detector data $\mathbf{X}$ into Eq. (1). As a practical matter, the precise choice of what $\mathbf{Y}$ to use has a large effect on the quality of the corrected images that are produced by applying the method of this paper. The issues considered when seeking an appropriate $\mathbf{Y}$ constitute the computational parameter space referred to in Section 1. Space limitations prevent us from presenting results on all the factors we have explored. However, some of these are worthy of mention here, as they strongly affect the quality of results.

A previously reported result is that, in practice so far, high-quality corrected images are obtained by applying the method explored here only if the $N_p \times N_t$ training set $\mathbf{Y}$ used for generating the deconvolution operator has the property $N_t \gg N_p$. Probable reasons for this phenomenon were discussed at length in the earlier report, so the explication is not repeated here. We reiterate only the observation that the key factor apparently is the dependence of the singular value spectrum—from which both the condition number and the effective rank are derived—of $\hat{\mathbf{Y}}$ on N_t. Not shown here are the results of 2D studies on this phenomenon, which gave the expected result that the performance of the filtering operation has the same dependence on N_t as was seen for the 3D case (for the corrected images presented in this report, $N_t/N_p = 10$–23, while significantly poorer results are obtained when the ratio is smaller than this).

Another issue studied is the dependence on the functional form of the temporal variation assigned to the FEM nodes during filter generation. A seeming limitation on the use of sinusoids with irrational frequency ratios is that, as the number of nodes increases, an inconveniently large number of very small time steps may become necessary for unambiguous discrimination of all the modulation frequencies. An alternative approach that was tried was to assign an independent uniformly distributed random fluctuation to each node. In principle, the $\mathbf{Y}$'s and $\mathbf{X}$'s resulting from this type of optical parameter fluctuation should produce $\mathbf{F}$'s that perform as well as those derived from sinusoidally varying properties. In practice, however, we have found that for any given N_t, the results obtained by using the random fluctuations $\mathbf{F}$(i.e., $\mathbf{F}_{\text{ran}}$) are not as good as those produced by the sinusoidal fluctuations $\mathbf{F}$(i.e., $\mathbf{F}_{\text{sin}}$). Preliminary analysis suggests that this result is attributable to differences between the singular value spectra of $\hat{\mathbf{Y}}_{\text{ran}}$ and $\hat{\mathbf{Y}}_{\text{sin}}$.

The relative (i.e., spatially invariant or increasing with depth) and absolute amplitudes of the sinusoidal modulations assigned to the mesh nodes are additional computation-space parameters we have examined. As a practical matter, it has so far been found that the best results are obtained from deconvolution operators generated when the amplitude is spatially invariant and not more than a few percent of the mean value. Both effects can be understood in

terms of considerations that were discussed in Ref. 2: Reducing the amplitude near the boundary results in a $\mathbf{Y}$ that does not constitute a representative sampling of the optical-parameter space in which the target media (i.e., those to which the correction algorithm are applied) may reside; and if the amplitude is increased too much, either uniformly or increasingly with depth, then the mathematical relation between the training set media and their uncorrected reconstructed images cannot be approximated with sufficient accuracy by a linear transformation.

2. Computational Effort

The filter-generation method outlined in Subsection 2.A is theoretically independent of not only the functional form of the mesh nodes' optical parameter fluctuations, as described in the Subsection 4.B.1, but also on the algorithm used for reconstruction of the uncorrected images. That is, the factors of $\mathbf{W}$ and $\mathbf{W}^+$ that appear in Eqs. (1) and (2) simply refer to *an* unspecified imaging operator. An important caveat, however, is that the algorithm used for inverse-problem computations in the filter-generation step must be the same as the one used to reconstruct the images that will subsequently be corrected by application of the filter. Given that computation of deconvolution operators that perform well presently requires generation of training sets containing $>10^4$ images, it is clear that the correction method presented here is practicable only if the reconstruction algorithm used is intrinsically capable of producing many images in a short time. This capability is definitely present in linear reconstruction methods such as the algorithm discussed in Subsection 2.D. On the other hand, it is not certain whether more labor-intensive nonlinear approaches that have been taken for DOT image reconstruction can be accelerated to the degree that would be required.

C. Future Directions

1. The training set $\mathbf{Y}$ will be expanded to include simultaneous fluctuations of μ_a and μ_s' at each FEM mesh node. The premise is that interparameter cross talk can be regarded as a particular form of information spread. That being so, it is our expectation that a deconvolution operator incorporating information on both coefficients will appreciably reduce the degree of cross talk.

2. In another development effort, we plan to explore procedures that will combine spatial deconvolution with techniques for suppressing ringing, noise, and numerical error artifacts.

3. Incorporation of other types of regularization into imaging operators, particularly the use of depth-dependent regularization, is worthy of exploration. As indicated earlier, it is expected that results such as those plotted in Figs. 4(a), and 5(a) and 5(b) can be used to guide the determination of the optimal regularization parameter depth dependence for a given medium geometry and S–D configuration.

4. With minor modifications, the reasoning outlined in Subsection 2.A can be used to derive a transformation that should produce a corrected image directly from a set of detector data, eliminating the intermediate step of reconstructing an image via the algorithm discussed in Subsection 2.D, or any other. The idea here is to replace the equation relating the matrix of medium properties ($\mathbf{Y}$) to one of corresponding reconstructed images ($\hat{\mathbf{Y}}$) with one that relates $\mathbf{Y}$ to the matrix of corresponding detector readings ($\mathbf{X}$). As mentioned in Subsection 2.A, the definition of the spatial deconvolution operator ($\mathbf{F}$) is expressed by $\mathbf{Y} = \mathbf{F}\hat{\mathbf{Y}}$, and the reconstructed images corresponding to $\mathbf{Y}$ are given in theory by $\hat{\mathbf{Y}} = \mathbf{W}^+\mathbf{X}$. Combining these two matrix equations, we obtain $\mathbf{Y} = \mathbf{F}\mathbf{W}^+\mathbf{X} \equiv \mathbf{F}'\mathbf{X}$, where $\mathbf{F}$ is the spatial deconvolution operator used to produce the results presented above and in Refs. 1 and 2. Formally, the reconstruction-free transformation is $\mathbf{F}' = \mathbf{Y}\mathbf{X}^+$, or

$$\mathbf{F}' = \mathbf{Y}\mathbf{X}^T(\mathbf{X}\mathbf{X}^T)^{-1}, \tag{9}$$

whereas for a target medium $\mathbf{z}$ with corresponding detector data $\mathbf{v}$, the deconvolved image is $\hat{\mathbf{z}} = \mathbf{F}'\mathbf{v} \approx \mathbf{z}$, or

$$\hat{\mathbf{z}}' = \left[\mathbf{Y}\mathbf{X}^T(\mathbf{X}\mathbf{X}^T)^{-1}\right]\mathbf{v}. \tag{10}$$

Comparison of Eqs. (1) and (2) with Eqs. (9) and (10) reveals that the only difference between the pairs is that the latter contains no reference to a $\mathbf{W}$ operator. The explicit formal dependences on the training set $\mathbf{Y}$, and the corresponding forward-problem solutions $\mathbf{X}$ are precisely the same in both groups of equations.

The decision to refer to the matrix $\mathbf{Y}$ as a training set was taken to suggest an analogy with the field of artificial neural networks. In the artificial-neural-network community, it is known that any problem that can be solved by training a network is also solvable via conventional nonlinear error minimization algorithms.[36] In the preceding paragraph, the transformation matrix $\mathbf{F}'$ is the solution to a linear error minimization problem, and an additional subject worthy of exploring is the derivation of higher-order relations between $\mathbf{Y}$ and $\mathbf{X}$.

In the preliminary tests carried out so far, the use of Eq. (10) did not produce satisfactory images. This was neither unexpected nor discouraging, however, in light of the amount of empirical fine-tuning (Subsection 4.B) that went into obtaining results of the quality presented here by using the algorithm outlined in Subsection 2.A. Nevertheless, we believe that this approach is worthy of additional study.

This research was supported by the National Institutes of Health under grants R21-HL67387, R21-DK63692, R41-CA96102, and R43-NS49734, and by the U.S. Army under grant DAMD017-03-C-0018.

References and Notes

1. R. L. Barbour, H. L. Graber, Y. Xu, Y. Pei, and R. Aronson, "Strategies for imaging diffusing media," Transp. Theory Stat. Phys. **33,** 361–371 (2004).

2. H. L. Graber, Y. Xu, Y. Pei, and R. L. Barbour, "Qualitative and quantitative improvement of optical tomographic reconstructed images via spatial deconvolution: three-dimensional case," Appl. Opt. **44,** 941–953 (2005).
3. S. Colak, M. van der Mark, G. W.'t Hooft, J. Hoogenraad, E. van der Linden, and F. Kuijpers, "Clinical optical tomography and NIR spectroscopy for breast cancer detection," IEEE J. Sel. Top. Quantum Electron. **5,** 1143–1158 (1999).
4. V. Ntziachristos, A. Yodh, M. Schnall, and B. Chance, "Concurrent MRI and diffuse optical tomography of breast after Indocyanine Green enhancement," Proc. Natl. Acad. Sci. USA **97,** 2767–2772 (2000).
5. B. W. Pogue, S. P. Poplack, T. O. McBride, W. A. Wells, K. S. Osterman, U. L. Osterberg, and K. D. Paulsen, "Quantitative hemoglobin tomography with diffuse near-infrared spectroscopy: pilot results in the breast," Radiology **218,** 261–266 (2001).
6. H. Jiang, Y. Xu, N. Iftimia, J. Eggert, K. Klove, L. Baron, and L. Fajardo, "Three-dimensional optical tomographic imaging of breast in a human subject," IEEE Trans. Med. Imaging **20,** 1334–1340 (2001).
7. D. A. Boas, G. Strangman, J. P. Culver, R. D. Hoge, G. Jasdzewski, R. A. Poldrack, B. R. Rosen, and J. B. Mandeville, "Can the cerebral metabolic rate of oxygen be estimated with near-infrared spectroscopy?" Phys. Med. Biol. **48,** 2405–2418 (2003).
8. H. Obrig and A. Villringer, "Beyond the visible—imaging the human brain with light," J. Cereb. Blood Flow Metab. **23,** 1–18 (2003).
9. A. Y. Bluestone, G. Abdoulaev, C. H. Schmitz, R. L. Barbour, and A. H. Hielscher, "Three-dimensional optical tomography of hemodynamics in the human head," Opt. Express **9,** 272–286 (2001), http://www.opticsexpress.org.
10. J. C. Hebden, "Advances in optical imaging of the newborn infant brain," Psychophysiology **40,** 501–510 (2003).
11. H. L. Graber, Y. Pei, and R. L. Barbour, "Imaging of spatiotemporal coincident states by DC optical tomography," IEEE Trans. Med. Imaging **21,** 852–866 (2002).
12. B. W. Pogue, T. O. McBride, U. L. Osterberg, and K. D. Paulsen, "Comparison of imaging geometries for diffuse optical tomography of tissue," Opt. Express **4,** 270–286 (1999), http://www.opticsexpress.org.
13. S. Prince, V. Kolehmainen, J. P. Kaipio, M. A. Franceschini, D. Boas, and S. R. Arridge, "Time-series estimation of biological factors in optical diffusion tomography," Phys. Med. Biol. **48,** 1491–1504 (2003).
14. V. Kolehmainen, S. Prince, S. R. Arridge, and J. P. Kaipio, "State-estimation approach to the nonstationary optical tomography problem," J. Opt. Soc. Am. A **20,** 876–889 (2003).
15. V. A. Markel and J. C. Schotland, "Effects of sampling and limited data in optical tomography," Appl. Phys. Lett. **81,** 1180–1182 (2002).
16. Y. Pei, H. L. Graber, and R. L. Barbour, "Normalized-constraint algorithm for minimizing inter-parameter crosstalk in DC optical tomography," Opt. Express **9,** 97–109 (2001), http://www.opticsexpress.org.
17. T. Budinger, F. Wehrli, S. M. Blumenfeld, F. A. Grunbaum, R. M. Henkelman, P. C. Lauterbur, W. Loeffler, F. Natterer, S. J. Nelson, L. Shepp, R. G. Shulman, B. M. W. Tsui, S. T. Weidman, R. L. Riemer, and C. M. Pechura, *Mathematics and Physics of Emerging Biomedical Imaging* (National Academy Press, Washington, D.C., 1996), p. 138.
18. Y. Pei, H. L. Graber, and R. L. Barbour, "Influence of systematic errors in reference states on image quality and on stability of derived information for dc optical imaging," Appl. Opt. **40,** 5755–5769 (2001).
19. It is recognized that techniques for experimental estimation of the bulk or background properties of target media will not yield perfectly accurate results. Consequently, a full characterization of the spatial deconvolution method will require consideration of cases in which the properties of the media used for the computations of $\mathbf{I}$ and $\mathbf{I}_0$ differ. For reasons of space limitations, the influence of disparities between the media on the accuracy of the deconvolved image is deferred to future publications in this series.
20. When images are reconstructed from experimental or clinical data, typically there is an appreciable difference between $\mathbf{I}_0$ and $\mathbf{I}_r$. But as shown in Ref. 18, the normalized-difference method is highly robust to disparities between the media that yield these measurement vectors. Then it is expected that introducing a difference between $\mathbf{I}_0$ and $\mathbf{I}_r$ will not affect the performance of the spatial deconvolution algorithm. Direct tests of this hypothesis will be another subject presented in future publications.
21. K. D. Paulsen and H. Jiang, "Spatially-varying optical property reconstruction using a finite element diffusion equation approximation," Med. Phys. **22,** 691–702 (1995).
22. Z. H. Cho, J. P. Jones, and M. Singh, *Foundation of Medical Imaging* (Wiley, New York, 1993), p. 80.
23. R. Archibald and A. Gelb, "A method to reduce the Gibbs ringing artifact in MRI scans while keeping tissue boundary integrity," IEEE Trans. Med. Imaging **21,** 305–319 (2002).
24. D. Contini, H. Liszka, A. Sassaroli, and G. Zaccanti, "Imaging of highly turbid media by the absorption method," Appl. Opt. **35,** 2315–2324 (1996).
25. J. Zhou, J. Bai, and P. He, "Spatial location weighted optimization scheme for DC optical tomography," Opt. Express **11,** 141–150 (2003), http://www.opticsexpress.org.
26. B. W. Pogue, T. O. McBride, J. Prewitt, U. L. Österberg, and K. D. Paulsen, "Spatially variant regularization improves diffuse optical tomography," Appl. Opt. **38,** 2950–2961 (1999).
27. J. P. Culver, V. Ntziachristos, M. J. Holboke, and A. G. Yodh, "Optimization of optode arrangements for diffuse optical tomography: a singular-value analysis," Opt. Lett. **26,** 701–703 (2001).
28. Y. Pei, F.-B. Lin, and R. L. Barbour, "Modeling of sensitivity and resolution to an included object in homogeneous scattering media and in MRI-derived breast maps," Opt. Express **5,** 203–219 (1999), http://www.opticsexpress.org.
29. J. P. Culver, R. Choe, M. J. Holboke, L. Zubkov, T. Durduran, A. Slemp, V. Ntziachristos, B. Chance, and A. G. Yodh, "Three-dimensional diffuse optical tomography in the parallel plane transmission geometry: evaluation of a hybrid frequency domain/continuous wave clinical system for breast imaging," Med. Phys. **30,** 235–247 (2003).
30. J. Chang, H. L. Graber, R. L. Barbour, and R. Aronson, "Recovery of optical cross-section perturbations in dense scattering media using transport-theory-based imaging operators and steady-state simulated data," Appl. Opt. **35,** 3963–3978 (1996).
31. J. Chang, H. L. Graber, and R. L. Barbour, "Dependence of image quality on image operator and noise for optical diffusion tomography," J. Biomed. Opt. **3,** 137–144 (1998).
32. R. L. Barbour, H. L. Graber, Y. Pei, S. Zhong, and C. H. Schmitz, "Optical tomographic imaging of dynamic features of dense-scattering media," J. Opt. Soc. Am. A **18,** 3018–3036 (2001).
33. V. E. Pera, E. L. Heffer, H. Siebold, O. Schütz, S. Heywang-Köbrunner, A. Götz, A. Heinig, and S. Fantini, "Spatial second-derivative image processing: an application to optical mammography to enhance the detection of breast tumors," J. Biomed. Opt. **8,** 517–524 (2003).
34. Q. Zhang, J. J. Stott, T. J. Brukilacchio, A. Li, T. Chaves, G. Boverman, T. Wu, M. Chorlton, T. Rafferty, R. H. Moore, D. B. Kopans, and D. A. Boas, "Preliminary study of the breast's bulk optical properties using a co-registered tomographic x-ray

and optical breast imaging system," presented at OSA Biomedical Topical Meetings and Tabletop Exhibit, Miami Beach, Fla., 14–17 April 2004.
35. S. Suzuki and S. Yamaguchi, "Comparison between an image reconstruction method of filtering backprojection and the filtered backprojection method," Appl. Opt. **27,** 2867–2870 (1988).
36. C. M. Bishop, *Neural Networks for Pattern Recognition* (Oxford U. Press, Oxford, UK, 1995).